R NUCLEAR RESEARCH

CERN-EP/89-121
September 15th, 1989

MEASUREMENTS OF THE NUCLEON STRUCTURE FUNCTION IN THE RANGE $0.002 < x < 0.17$ AND $0.2 < Q^2 < 8$ GeV^2 IN DEUTERIUM, CARBON AND CALCIUM

The European Muon Collaboration

Aachen[1], CERN[2], DESY (Hamburg)[3], Freiburg[4], Hamburg (University)[5], Kiel[6], LAL (Orsay)[7], Lancaster[8], LAPP (Annecy)[9], Liverpool[10], Marseille[11], Mons[12], MPI (München)[13], Oxford[14], RAL (Chilton)[15], Sheffield[16], Torino[17], Uppsala[18], Warsaw[19], Wuppertal[20]

M. Arneodo[17], A. Arvidson[18], J.J. Aubert[11], B. Badelek[19a)], J. Beaufays[2], C.P. Bee[10], C. Benchouk[11], G. Berghoff[1], I.G. Bird[8b)], D. Blum[7], E. Böhm[6], X. de Bouard[9+], F.W. Brasse[3], H. Braun[20], C. Broll[9+], S.C. Brown[10c)], H. Brück[20d)], H. Calén[18], J.S. Chima[15e)], J. Ciborowski[19a)], R.Clifft[15], G. Coignet[9], F. Combley[16], J. Coughlan[8f)], G.d'Agostini[11], S. Dahlgren[18], I. Derado[13], T. Dreyer[4], J. Drees[20], M. Düren[1], V. Eckardt[13], A. Edwards[20g)], M. Edwards[15], T. Ernst[4], G. Eszes[9h], J. Favier[9], M.I. Ferrero[17], J. Figiel[5i)], W. Flauger[3], J. Foster[16j)] E. Gabathuler[10], J. Gajewski[5a)], R. Gamet[10], N. Geddes[14f)], P. Grafström[18k)], L. Gustafsson[18], J. Haas[4], E. Hagberg[18], F.J. Hasert[11)], P. Hayman[10], P. Heusse[7], M. Jaffre[7], A. Jacholkowska[2m)], F. Janata[5n)], G. Jancso[13h)], A.S. Johnson[14o)], E.M. Kabuss[4b)], G. Kellner[2], A. Krüger[17], J. Krüger[3], S. Kullander[18], U. Landgraf[4], D. Lanske[1], J. Loken[14], K. Long[14f)], M. Maire[9], P. Malecki[13], A. Manz[13], S. Maselli[13], W. Mohr[4], F. Montanet[11], H.E. Montgomery[2p)], E. Nagy[9h)], J. Nassalski[19q)], P.R. Norton[15], F.G. Oakham[15r)], A.M. Osborne[2], C. Pascaud[7], B. Pawlik[13], P. Payre[11], C. Peroni[17], H. Peschel[20], H. Pessard[9], J. Pettingale[10], B. Pietrzyk[11], B. Poensgen[5], M. Pötsch[20], P. Renton[14], P. Ribarics[9h)], K. Rith[4b)], E. Rondio[19a)], A. Sandacz[19q)], M. Scheer[1], A. Schlagböhmer[4s)], H. Schiemann[5], N. Schmitz[13], M. Schneegans[9], M. Scholz[1], M. Schouten[13], T. Schröder[4], K. Schultze[1], T. Sloan[8], H.E. Stier[4], M. Studt[5], G.N. Taylor[14t)], J.M. Thenard[9], J.C. Thompson[15], A. de la Torre[5u)], J. Toth[9h)], L. Urban[1], L. Urban[9h)], W. Wallucks[4], M. Whalley[16v)], S. Wheeler[16], W.S.C. Williams[14], S.J. Wimpenny[10w)], R. Windmolders[12], G. Wolf[13].

(Submitted to Nuclear Physics B)

ABSTRACT

Small angle scattering of 280 GeV positive muons by deuterium, carbon and calcium has been measured at scattering angles down to 2 mrad. The nucleon structure function F_2 extracted from deuterium does not show a significant x dependence in the measured range of Q^2 and its Q^2 dependence is linear in log Q^2. For calcium, a depletion of F_2 is observed at low x by 30% as compared with the values at $x = 0.1$ where F_2(Ca) and F_2(D) are not significantly different. This depletion is attributed to shadowing. The carbon structure function exhibits a similar, but less pronounced, x dependence. Such behaviour is observed to be independent of Q^2. The data are consistent with those obtained from other charged lepton experiments both at similar and higher values of x and Q^2 and considerably extend the range of the measurements down to the low values of x to be measured in forthcoming experiments at HERA.

Addresses

1) III Physikalisches Institut A, Physikzentrum, RWTH, D-5100 Aachen, FRG.
2) CERN, CH-1211 Geneva 23, Switzerland.
3) DESY, D-2000 Hamburg, FRG.
4) Fakultät für Physik, Universität Freiburg, D-7800 Freiburg, FRG.
5) II Institut für Experimentalphysik, Universität Hamburg, D-2000, FRG.
6) Institut für Kernphysik, Universität Kiel, D-2300 Kiel, FRG.
7) Laboratoire de l'Accélérateur Linéaire, Université de Paris-Sud, F-914005 Orsay, France.
8) Department of Physics, University of Lancaster, Lancaster LA1 4YB, UK.
9) Laboratoire d'Annecy-le-Vieux de Physique des Particules, B.P. 110, F-74941, Annecy-le-Vieux, Cedex, France.
10) Department of Physics, University of Liverpool, Liverpool L69 3BX, UK.
11) Centre de Physique des Particules, Faculté des Sciences de Luminy, 13288 Marseille, France.
12) Faculté des Sciences, Université de Mons, B-7000 Mons, Belgium.
13) Max-Planck-Institut für Physik and Astrophysik, D-8000 München, FRG.
14) Nuclear Physics Laboratory, University of Oxford, Oxford OX1 3RH, UK.
15) Rutherford - Appleton Laboratory, Chilton, Didcot OX1 0QX, UK.
16) Department of Physics, University of Sheffield, Sheffield S3 7RH, UK.
17) Istituto di Fisica, Università di Torino, I-10125, Italy.
18) Department of Radiation Science, University of Uppsala, S-75121 Uppsala, Sweden.
19) Physics Institute, University of Warsaw and Institute for Nuclear Studies, PL-00681 Warsaw, Poland, partly supported by CPBP.01.09.
20) Fachbereich Physik, Universität Wuppertal, D-5600 Wuppertal, FRG.

a) University of Warsaw, Poland.
b) Now at MPI für Kernphysik, Heidelberg, FRG.
c) Now at TESA S.A., Renens, Switzerland.
d) Now at DESY, Hamburg, FRG.
e) Now at British Telecom, London, UK.
f) Now at RAL, Chilton, Didcot, UK.
g) Now at Jet, Joint Undertaking, Abingdon, UK.
h) Permanent address: Central Research Institute for Physics, Hungarian Academy of Science, Budapest, Hungary.
i) Now at Institute of Nuclear Physics, Krakow, Poland.
j) Now at University of Manchester, UK.
k) Now at CERN, Genève, Switzerland.
l) Now at Krup Atlas Elektronik GmbH, Bremen, FRG.
m) Now at Laboratoire de l'Accélérateur Linéaire, Université de Paris-Sud, Orsay, France.
n) Now at Beiersdorf AG, Hamburg, FRG.
o) Now at SLAC, Stanford, California, USA.
p) Now at FNAL, Batavia, Illinois, USA.
q) Institute for Nuclear Studies, Warsaw, Poland.
r) Now at NRC, Ottawa, Canada.
s) Now at GEI, Darmstadt, FRG.
t) Now at University of Melbourne, Parkville, Victoria, Australia.
u) Now at Universidad Nacional, Mar del Plata, Argentina.
v) Now at University of Durham, UK.
w) Now at University of California (Riverside), USA.
+) Deceased.

1. INTRODUCTION

Over the past decade our knowledge of the nucleon structure functions or the parton distributions in the nucleon has greatly improved. Since the pioneering MIT/SLAC measurements of highly inelastic electron-proton scattering [1], a vast amount of data has been accumulated from high statistics neutral ($\nu,\bar{\nu}$) and charged (e,μ) lepton scattering experiments [2].

The differential cross section for deep inelastic scattering (DIS) of a charged lepton from an unpolarised nucleon (neglecting the lepton mass and the Fermi motion of the target nucleon) can be written in the one-photon exchange approximation (fig.1):

$$\frac{d^2\sigma(x,Q^2)}{dQ^2dx} = \frac{4\pi\alpha^2}{Q^4}\left[(1-y-\frac{Mxy}{2E})\frac{F_2(x,Q^2)}{x} + y^2F_1(x,Q^2)\right] \tag{1}$$

$$= \frac{4\pi\alpha^2}{Q^4}\frac{F_2(x,Q^2)}{x}\left\{1-y-\frac{Mxy}{2E}+\frac{y^2(1+\frac{4M\,x}{Q^2})}{2\left[1+R(x,Q^2)\right]}\right\}.$$

Here F_1 and F_2 (or R and F_2) are the structure functions of the nucleon, $x = Q^2/2M\nu$, $y = \nu/E$ with E, ν, Q^2 the incident beam energy, the energy transfer in the laboratory frame, the four momentum transfer to the virtual photon, respectively and M is taken to be the proton mass. The function R is the ratio of the photoabsorption cross sections for longitudinally and transversely polarised virtual photons.

In the quark-parton model (QPM), valid at large Q^2, the structure function F_2 is given by

$$F_2 = \sum_f e_f^2\, x\left[q_f(x) + \bar{q}_f(x)\right], \tag{2}$$

where e_f is the charge of the quark (antiquark) of flavour f which has a probability distribution $q_f(x)$ ($\bar{q}_f$). For an isoscalar target this reduces to

$$F_2 = \frac{1}{2}(F_2^p + F_2^n) = \frac{5}{18}\,x\,(u+\bar{u}+d+\bar{d}+s+\bar{s}+c+\bar{c}) + \frac{1}{6}\,x\,(c+\bar{c}-s-\bar{s}). \tag{3}$$

Here u, d, s, c ($\bar{u}$, $\bar{d}$, $\bar{s}$, $\bar{c}$,) are the up, down, strange and charmed quark (antiquark) distributions inside a nucleon. In the naive quark-parton model they are functions of x only (scaling); the observed weak Q^2 dependence comes from the quantum chromodynamics (QCD) corrections to the QPM.

According to QCD, at low values of x ($x \sim 10^{-4}$) and at large values of Q^2 a nucleon consists predominantly of gluons and sea quarks. Their densities grow rapidly in the limit $x \to 0$ thus leading to possible spatial overlap and to interactions between the partons. In this region the (virtual) photon - nucleon interaction can be described both by perturbative QCD and also by conventional Regge pole models for hard processes.

Due to the conservation of the electromagnetic current, F_2 must vanish as Q^2 goes to zero. This implies that scaling should not be a valid concept in the region of very low Q^2. The rise of F_2 with Q^2 is sometimes termed the "approach to scaling". The exchanged photon is then almost real and the close similarity of real photonic and hadronic interactions justifies the use of the Vector Meson Dominance (VMD) concept [3,4]. In the language of perturbation theory this concept is equivalent to a statement that a physical photon spends part of its time as a "bare", point-like photon, and part as a virtual hadron(s). In the simplest form of VMD, the hadronic component is identified with the vector mesons ρ, ω and ϕ. The photon-hadron interaction is then similar in nature to the interaction between hadrons.

In this paper measurements of the nucleon structure function F_2 are presented in the range $0.002 < x < 0.17$ and $0.2 < Q^2 < 8$ GeV^2 which are suitable for investigating the onset of scaling. Comparison of the data from calcium, carbon and deuterium targets allows the influence of the nuclear medium to be studied. The bound nucleon structure function has previously been observed to be reduced (for $x < 0.1$) relative to that measured from free nucleons [3,4]. This effect is known as shadowing i.e. the cross section per nucleus is less than A times the single nucleon cross section, where A is the number of nucleons in the nucleus. The Q^2 dependence of the ratio of F_2 measured in a heavy nuclear target to that in deuterium allows a study to be made of the interplay between the VMD behaviour of the virtual photon and its purely electromagnetic interactions.

The results presented here considerably extend previous measurements from both charged lepton or neutrino beam in this kinematic region [5,6,7,8,9]. It should be noted that our data are in a Q^2 range which is covered by electron accelerators. However, much smaller values of x are accessible in this experiment due to the higher muon beam energy. The kinematic region of the data overlaps in x that which will be studied in future HERA experiments. The measurements of the absolute values of F_2 from quasi free nucleons in deuterium are therefore useful to constrain parameterisations and predictions of the quark distribution functions which are being made for comparison with such future experiments [10].

2. EXPERIMENTAL APPARATUS

The experiment was performed in the M2 positive muon beam at the CERN SPS (experiment number NA28). The data were collected in parallel with

those from another EMC experiment (NA9). The apparatus consisted of three main parts, the beam spectrometer, the vertex spectrometer and the forward spectrometer. The general layout of the NA28 experiment is shown in figure 2 and parameters of the detectors relevant to the small angle scattering measurements are listed in tables 1 and 2.

The momentum and the position of the incident muon were measured with a beam momentum spectrometer (BMS) and a set of hodoscopes (BHA and BHB). The target was placed inside the vertex spectrometer consisting of a large superconducting magnet, the vertex spectrometer magnet (VSM), with a streamer chamber inside, surrounded by wire chambers and Cerenkov counters. It was used for measurements of identified hadrons emitted both forward and backward in the centre of mass system. The scattered muon and forward going fast hadrons were detected in the forward spectrometer (FS) consisting of a large aperture dipole magnet, the forward spectrometer magnet (FSM), surrounded by wire chambers. Muons were identified by tracks found in the wire chambers situated behind a 2 m thick iron absorber at the end of the spectrometer. A small angle trigger, consisting of scintillator hodoscopes and a dedicated trigger processor, was introduced, together with some chambers to allow the measurement of outgoing muons with small scattering angles. A detailed description of the spectrometer can be found in [11, 12] and of the small angle trigger in [13, 14].

In the following we describe only those parts of the apparatus that were important for the NA28 experiment. The coordinate system used throughout this paper is right handed with the x-axis pointing downstream along the beam, the y-axis horizontal and the z-axis pointing vertically upwards.

2.1 The Muon Beam

The muon beam was generated from the in-flight decay of charged pions and kaons, emitted in the interactions of protons with a primary target. The nominal beam energy used in the NA28 experiment was 280 GeV, with an r.m.s. momentum spread of 12.6 GeV. During this experiment positive muons were used at an intensity of 10^7 per pulse of duration 1.5 s and repetition rate 0.1 Hz. The beam cross section had an r.m.s. spread of 15-20 mm and the r.m.s. divergences were 0.2-0.4 mrad horizontally and 0.4-0.5 mrad vertically.

The momentum of each beam particle was measured in the BMS (not shown in fig.2) and the position in front of the target by the scintillation hodoscopes BHA and BHB. The hodoscopes BHA and BHB were 5 m apart and placed immediately upstream of the target. Each hodoscope consisted of 5 planes and their components are described in table 1. In addition, three single element scintillation counters S_1, S_2 and S_3 separated by 6 m were located 25 m upstream of the target. The triple coincidence $S=S_1S_2S_3$ was used as a time reference and as a strobe for the trigger processor.

2.2 Targets

The targets used were (liquid) deuterium, carbon and calcium. The target container for the deuterium was a 100 cm long cylinder mounted inside the streamer chamber of the vertex spectrometer. As the streamer chamber could not easily be dismounted the two solid targets had to be placed at the entrance of the magnet. Parameters characterizing the targets are given in table 3. Data were also acquired without any solid target and with an empty deuterium container in order to assess the background.

2.3 The Forward Spectrometer

The basic ingredients of the forward spectrometer beside the magnet were two sets of wire chambers (one in front of and one behind the magnet) for momentum and position determination and the iron absorber followed by wire chambers allowing the identification of muons.

The lever arm in front of the FSM consisted of two groups of chambers 5 m apart, P0C/PV2 at the exit of the VSM and P0AB/W12 just in front of the FSM. The multiwire proportional chambers P0A-C, which were located in the beam region, were used to measure tracks at small scattering angles whereas the drift chambers W12 and the large proportional chamber PV2, desensitized in the beam region, extended the measurements to large angles. The chambers P0A-C were especially designed to work in high particle fluxes up to 5×10^7 muons/s. Each of these chambers, covering the desensitized regions of the larger chambers, had a sensitive area of about 15 cm in diameter and a wire spacing of 1 mm. Two planes, measuring the same coordinate, were displaced by 0.5 mm to obtain a resolution of 0.5 mm.

The lever arm behind the FSM consisted of two blocks of detectors for the large angle measurement. The first block, W3, had drift chambers and was located just behind the FSM. The second block, W45, 6 m downstream of W3, consisted of drift chambers interleaved with the multiwire proportional chambers, P45 which were sensitive in the beam region and were used to measure tracks scattered at small angles. The 8 planes of P45 had wires spaced by 2.02 mm and were roughly circular with a diameter of 90.5 cm.

The forward spectrometer magnet was a conventional dipole magnet. The aperture was 1×2 m^2 and the length along the beam was 4.3 m. The bending power was 5.2 Tm at a current of 5000 A. Inside the magnet there were three proportional chambers P1, P2 and P3, filling the complete aperture, which were used for track reconstruction in the magnet.

The remaining parts of the forward spectrometer were the iron absorber and the large drift chambers, W67, used for muon identification. The absorber had a depth along the beam of 2 m and it had a hole, 15 cm wide and 15 cm high, to allow the beam to pass through. Outside this hole the produced hadrons were absorbed and only muons were expected to reach the W67 chambers downstream of the absorber.

There were no wire chambers behind the absorber to measure tracks passing through or near the absorber hole since the W67 chambers were desensitized in the beam region. Part of this gap was covered by the small scintillator hodoscope H5 at the end of the spectrometer. This hodoscope consisted of two planes with a sensitive area of 19×20 cm^2 and with 5 and 4 elements respectively. Fast positive tracks at small scattering angles which passed through the hole, were assumed to be scattered muons. Correction for the hadron contamination of these events was made by Monte Carlo, as discussed below.

2.4 The Trigger

Four small scintillator hodoscopes were added to the forward spectrometer to form the small angle trigger. Two of them, BHC and BHD, were located in front of the absorber, the others, BHD and BHE, behind the absorber and interleaved with the wire chambers of the W67 block. Specifications of the hodoscopes are given in table 1. BHC was mounted together with BHD on the upstream wall of the absorber. BHC was a two-dimensional matrix made of 144 cuboids each having a size of 1.45×1.45×0.5 cm^3 and mounted with a small overlap to cover a sensitive area of 16.8×16.8 cm^2 facing the beam. The other hodoscopes consisted of conventional scintillator stripes.

The trigger was formed by the signals from the counters S_1, S_2 and S_3 and the hodoscopes BHA-BHF in a dedicated trigger processor termed SAIT, an acronym for Small Angle Interaction Trigger. The purpose of the SAIT was to measure the track of the incoming muon in the hodoscopes BHA and BHB, to extrapolate the track through the two magnets to the hodoscopes BHC-BHF, and to compare the extrapolated track coordinates with the measured hits. The decision was then made whether the hits corresponded to a muon track scattered by more than the minimum desired angle. The processing time varied between 60 and 100 ns. This allowed the trigger to be used in beam intensities up to 10^7 muons/s. The very short decision time was mainly due to the fact that pattern matching was used instead of numerical calculations of the scattering angle.

The principle of the SAIT, more details of which can be found in ref.13, is illustrated in figure 3. A beam particle was identified by the S coincidence signal which initiated the processing. Firstly, a check was made to see if the hits in BHA and BHB were consistent with an incoming track that could be extrapolated to BHC-BHF. A valid track meant that there was one and only one hit per plane in BHA and BHB. If the information was insufficient to define the track, the SAIT was reset so that it was ready for a new event.

Secondly, a check was made if the track defined by BHA and BHB pointed to an element within the permitted range of BHC (see figure 3). The coordinates of this element were given by a linear extrapolation of the track coordinates. The spread in momentum of the beam particles was sufficiently small that the dispersion of the beam transverse dimensions could be neglected in this extrapolation. If this pointer in BHC was within the active area of the hodoscope, the processing continued.

Thirdly, a check was made as to whether the hits in BHC-BHF relative to the pointer position were consistent with a scattered muon. A "window", normally 4 or 5 elements wide (dotted in fig.3), was set up around the pointer position. For each hodoscope an accept/veto (A/V) combination was defined. If there was a hit in any of the elements within the window, the veto bit was set (V=1) and if there were hits outside the window, the accept bit was set (A=1). For each hodoscope there were thus 4 accept/veto combinations (A=1, V=0; A=1, V=1; A=0,V=1; A=0,V=0). This gave a total of 256 accept/veto combinations. The processor checked if the measured combination was consistent with an allowed one. A trigger signal was then produced.

The accept/veto combinations defining the small-angle trigger were chosen to be consistent with a muon scattered outside the windows and to allow for an inefficiency in one of the four hodoscopes or a hit by a delta electron or a hadron inside the windows. Table 4 shows the event rates for some of the trigger combinations and table 5 those used to define the event sample.

The window sizes chosen were usually 4×4 elements in BHC and the 5 horizontal or vertical elements in each of BHD, BHE and BHF. With this trigger condition we were able to select scattering angles down to 2 mrad, about a factor 5 below the minimum angle achieved with the standard EMC trigger [11, 12].

In addition, a trigger was defined by the S coincidence to detect unscattered beam particles. These were used to monitor the relative momentum calibration of the beam momentum spectrometer and the scattered muon spectrometers and to calibrate and monitor the efficiencies of hodoscopes and proportional chambers situated in the beam region.

3. DATA ANALYSIS

The analysis procedure follows closely that adopted for previous EMC structure function measurements [15,16,17]. However, the earlier measurements were not made in the beam region as in the present experiment and we shall concentrate our description on the novel features of the analysis. First we describe the reconstruction of the events, then follows a description of the Monte Carlo program used to correct the data.

3.1 Event Reconstruction

The momentum of the beam tracks was evaluated from hits in the hodoscopes of the BMS. The absolute accuracy determined by the precision in the measured magnetic field maps is estimated to be 0.4% and the accuracy relative to the measurements in the FSM, 0.05% (see below).

In the data recorded with the SAIT trigger the muons usually passed in the dead regions of most of the chambers. The reconstruction started in P45, the most downstream chambers which were sensitive in the beam region. The second step

was to find tracks in P0A and P0B upstream of the magnet. The tracks found in P0A/B were then compared with those found in P45 to see if it was possible to connect them into a complete track. The criteria used for this decision were based on the spatial distance between them in the middle of the magnet and the difference in their slopes in the non-bending plane. The background in P0A/B and P45 was very low which facilitated the track reconstruction. The chambers PV2 and P0C were not used at this stage since they were situated in the fringe field of the vertex magnet (see fig. 2). The momenta of the tracks were determined by means of a least squares fitting method based on a quintic spline model [18]. The momentum resolution was checked in simulations and found to be 1.5% at 280 GeV. In the final event reconstruction, the information from the wire chambers P0C and PV2 was also used. If a track in the forward spectrometer matched a line found in P0C or PV2, the spline fit was updated using this new information which occurred for about 75% of the tracks. This extra information improved the resolution of the vertex position.

The scattered muon identification was complicated by two facts: the large drift chambers, W67, downstream of the absorber were insensitive in their central region and the 15x15 cm^2 hole in the iron absorber which let the hadrons pass through. After all tracks displaying the charge opposite to the incident muon had been discarded the tracks were propagated through the absorber and matching hits were searched for in BHE, BHF and H5. Out of time tracks were rejected by checking the information from H5. If a track went in the hole in the absorber it was impossible to determine whether it was a muon or a hadron. It was estimated that about 60% of the scattered muons passed through this hole and for these muons it was necessary to determine the hadron contamination using Monte Carlo calculations.

It was also demanded that the scattered muon should satisfy the accept/veto combinations used in the trigger processor. In this check only the hits associated with the track were used. If more than one track fulfilled this condition then the one with the highest energy was selected to be the scattered muon. Monte-Carlo simulations showed that 0.7% of the muons were misidentified using this procedure.

The vertex resolution was about 20 cm on average for the coordinate along the beam axis and 0.5 mm for the transverse coordinate. The distributions of the longitudinal coordinates of the reconstructed vertices for deuterium, calcium and empty target data are shown in figure 4 for events before kinematic cuts.

3.2 Monte Carlo Simulations

The Monte Carlo program was used for the correction of the experimental acceptance, to estimate errors and to check the analysis procedure. The program has been described elsewhere [15] and we shall limit the discussion to the special features connected with small angle scattering.

The events were generated as follows: a beam track was randomly chosen from the measured beam sample, then the interaction point in the target was

chosen at random and a scattered muon generated. The hadronic final state was simulated according to the Lund fragmentation model [19]. All particles were propagated from the target through the apparatus taking into account multiple Coulomb scattering and energy loss in different media. Following this, hits in the various detectors were produced using the measured detector efficiencies. The hit pattern in BHA-BHF was checked for consistency with the hardware and software selections used for the trigger.

The Monte Carlo simulations were made in two versions, the "long chain" and the "short chain". In the long chain, hits from muons as well as from hadrons were generated and the events were then processed through the same analysis programs as the real data. In the short chain no hadrons were generated and the acceptance of an event was checked using geometrical extensions and efficiencies of all detector elements. Thus in the short chain, processing through the analysis programs was not necessary.

The long chain was used to check the analysis procedure and to determine the resolutions of momenta, scattering angles and vertex coordinates. These resolutions were then used to smear the parameters of the muons generated in the short chain. As an example a comparison between generated and reconstructed longitudinal coordinates of the interaction vertex is shown in figure 5.

Comparison of the long and the short chain results showed that the acceptance obtained from the short chain was in error by about 1%. The main part of this error was caused by hadrons which produced veto signals in the hodoscopes BHC-BHF. Other differences were due to a hadron and muon being close together and to misidentifying hadrons which passed through the hole in the iron absorber as muons. To compensate for these differences a correction was applied to the short chain calculations. The remaining error was small compared with other errors in the experiment and the short chain simulation was therefore sufficient. Five times more events than the aquired data were simulated, making the relevant contribution to the statistical error in F_2 small. Finally it should be mentioned that some background effects such as delta electrons and additional beam tracks could not be simulated. An account of how those effects are treated is given in section 3.6.

3.3 Momentum Calibration

As mentioned in section 2.4 a trigger was used to acquire data with unscattered beam particles. The momentum of these particles was measured in both the beam momentum and the scattered muon spectrometers. The two measurements were compared to give a relative calibration of the two spectrometers. Small time dependent differences of up to 0.3% were measured and the incoming muon momentum values were compensated for these differences. As a result of this procedure the errors came from two sources: from the uncertainty of the relative calibration of the beam momentum spectrometer and the scattered muon spectrometer (this error was estimated to be 0.05%) and from the precision of the absolute calibration of the two spectrometers (this error was 0.4% of the momentum value). Note that the latter error corresponds to the

case where the momentum calibration of the two spectrometers is wrong in the same direction, hence the effect on F_2 is small. By this method it was possible to improve considerably the systematic errors coming from the momentum calibration (see section 6).

3.4 Normalisation

As mentioned in section 2.4 the trigger demanded that there was one and only one hit in each beam hodoscope and that the extrapolated track pointed within the permitted area in the BHC hodoscope. The number of beam tracks satisfying these criteria was counted on scalers. The flux recorded must be corrected for all the software cuts applied to the beam tracks. This correction factor was determined by passing the data acquired with the beam trigger through the same analysis chain as the data from the small angle trigger. The fraction of beam tracks that passed all software cuts (~94%) was thus determined and the recorded flux was corrected by this fraction.

3.5 Efficiencies and Losses in the Event Reconstruction

Detailed investigations were made to understand the loss of events during their reconstruction. Below, an example of the losses at different stages of the reconstruction is given for a subsample of deuterium and carbon events.

Fraction of events...

i)	... from the data acquisition	100%
ii)	... with a reconstructed beam track	94%
iii)	... and with at least one reconstructed track in the FS	82%
iv)	... and with an identified muon	78%
v)	... and with a muon of the same charge as the beam track	77%
vi)	... and a muon fulfilling the trigger conditions	60%
vii)	... and with a reconstructed vertex	53%

The events lost at each stage of the reconstruction procedure were carefully studied. It was found that all the losses were satisfactorily reproduced in the Monte Carlo simulation except for ~2.5% of the deuterium events (~4% in carbon and calcium) without an observed outgoing track or identified muon. Since it was unclear whether a correction for these was necessary, no correction was applied and the effect was included as a systematic error.

The only loss for which a correction was necessary ocurred in the vertex reconstruction. Most of the losses at this stage were the background events, e.g. unscattered beam tracks which were poorly reconstructed in the scattered muon spectrometer or events coming from scattering in materials other than the target. No correction was necessary for this effect. However, the rest of the losses (<1%) were from genuine DIS events for which the vertex was not found. Long chain Monte Carlo studies showed an energy transfer dependence for these events. These losses were then corrected for and the uncertainty of this correction included in the systematic errors.

3.6 Efficiency of the Small Angle Trigger

As mentioned in section 2.4 the accept/veto combinations defining the trigger were chosen to allow for an inefficiency in one of the trigger hodoscope planes or for an extra hit inside the windows. Despite this there was a certain probability of inhibiting the trigger by background hits causing additional veto signals. Most of these hits were attributed to delta electrons and uncorrelated beam particles. Such a background was not included in the Monte Carlo simulation and was corrected for by the method described in this section. The method makes use of experimental data only and does not depend on any model of the background processes.

The correction was estimated by using the measured data acquired with 4×4,5,5,5 element window in BHC-BHF. Larger windows were imposed offline, up to 8×8,9,9,9. A new data set fulfilling the trigger condition was then selected with these larger windows, using only the hits associated with the muon track. The remaining hits were then added and the trigger condition imposed on all the hits in the event to determine the fraction of events rejected. This fraction was found to increase approximately linearly with the window size. The loss for the 4×4,5,5,5 window used in the trigger was estimated by extrapolating straight line fits to this increase, to zero window size (where the loss should be zero). The corrections for such losses were found to depend on the angle and the energy of the scattered muon and a table of correction factors was determined.

The correction factors for trigger combinations AAAA and 0AAA, corresponding to scattering in both horizontal and vertical directions, were 8%. For combinations AAAV and 0AAV corresponding to scattering in the horizontal plane the correction factor was 15%. For combinations AVVA and 0VVA corresponding to scattering in the vertical plane, the correction factor was 20%. The two last correction factors are larger than the first one due to the lower allowance for the extra hits for the respective trigger combinations. The trigger combinations used for the final selection of events were all similar to the first two types of combinations given above for the which the corrections were smallest (see section 5 and table 5).

3.7 Empty Target Subtraction

The events coming from the scattering off the target material were contaminated by events coming from the target walls for deuterium or other material along the beam. As mentioned in section 3.1, the vertex position was uncertain within 20 cm in the beam direction. Therefore it was not possible to remove the events originating in the target walls by defining a target "fiducial volume". Instead the distributions of event yields measured without the presence of the target were subtracted from the distributions of events from the sample.

For this purpose data had been recorded without a nuclear target and with the deuterium target vessel empty. These data were passed through the same analysis programs as those recorded with the target filled. The rate of

reconstructed events, for which the muon track satisfied the trigger condition and with a vertex point in the target region, was about 15% of the yield for deuterium (see fig.4). It was found that these events were situated at low x and low muon momenta. The applied cuts (section 5) brought the contribution of these background events down to 2.5% in all x,Q^2 bins without kinematical dependence. This contribution has been subtracted from the deuterium data. In the data taken with the carbon and calcium targets the contribution was neglible.

4. CROSS SECTIONS, RADIATIVE CORRECTIONS AND EXTRACTION OF THE NUCLEON STRUCTURE FUNCTION

The cross sections and structure functions were extracted for each target separately and then the ratios were calculated. This procedure was necessary since the two solid (C, Ca) and the liquid deuterium targets were placed at different positions along the beam and data were acquired at different times.

F_2 was extracted from the data in an iterative process following the same procedure as in previous analyses [15,16,17]. Firstly cuts (see section 5) were applied on the measured sample and events were summed up in finite size bins in Q^2 and x. The data were then normalized to the beam flux. The next step was to treat the events which had been simulated using the short chain Monte Carlo program. Each event was given a weight according to the cross section (eq. 1) and an initial F_2 parameterisation was assumed. The weight was then modified to include the radiative corrections (see below) and software losses which had not been accounted for in the simulation. The Monte Carlo events were submitted to the same cuts, summed up on the same grid in Q^2 and x and were finally normalized to the same beam flux as the experimental data. For each bin a modified value of the structure function was then computed:

$$F_2^{new}(x,Q^2) = \frac{N^{Data}_{\Delta x \Delta Q^2}}{N^{MC}_{\Delta x \Delta Q^2}} F_2^{old}(x, Q^2) \cdot \qquad (4)$$

The new values of the structure functions were then used to obtain new coefficients in the F_2 parameterisation by fitting that function to the data. The new F_2 parameterisation was used to compute new values of the radiative corrections. The procedure was then repeated a few times until convergence had been obtained.

In this procedure the value of $R=1.2(1-x)/Q^2$ was taken from a parameterisation of the CHIO data [7] in a similar x,Q^2 range. It was assumed to be independent of the nuclear atomic mass, which is consistent with current experimental data at higher values of x [20]. Note that the A independence of R implies that the ratio of cross sections measured on targets 1 and 2, σ^1/σ^2, is equal to the structure function ratio, F_2^1 / F_2^2.

The extracted values of F_2 were insensitive to the assumed value of R since the data are restricted to small values of y ($y < 0.55$, see section 5). The values of F_2 calculated from an assumed value $R=R_1$ can be adjusted to any other value of $R=R_2$ by applying the formula

$$\frac{F_2(R_1)}{F_2(R_2)} = \frac{1 - y + \frac{y^2}{2(1+R_2)}\left[1+\frac{4M^2x^2}{Q^2} - \frac{Mxy}{2E}\right]}{1 - y + \frac{y^2}{2(1+R_1)}\left[1+\frac{4M^2x^2}{Q^2} - \frac{Mxy}{2E}\right]}, \qquad (5)$$

neglecting the effect of R on the radiative corrections. For example, in this experiment if we take R=0 rather than the CHIO value mentioned above, F_2 changes by less than 2% over most of the kinematic range. However, this change increases by up to 17% at the lowest values of x for larger Q^2 values. These changes are in general small compared to the errors on the data.

The parameterisation fitted to F_2 at the final iteration is given in table 6.

The radiative corrections were necessary to extract the single photon exchange cross sections from the measured yield. These were calculated in the same way as in previous analyses [15,16,17] using the formulae of Tsai [21a] and iterative procedure of Mo and Tsai [21b]. In the range of this experiment the radiative tails from coherent elastic scattering from the nuclear targets (wide angle bremsstrahlung, WAB) give important contributions. The size of these contributions depends on nuclear form factors. For the ^{12}C and ^{40}Ca nuclei the Sum of Gaussian (SOG) parameterisation [22,23] was used. For deuterium the form factor parameterisation employed by Stein et al. [5] was adopted. The exact knowledge of the deuteron form factors is however not critical since the contribution from the elastic radiative tail is very low in the case of muon-deuteron scattering.

In addition to the coherent radiative tails from scattering on nuclei there are radiative tails from quasi elastic scattering on single nucleons. The suppression of such quasi elastic scattering at low Q^2, due to the Pauli exclusion principle, was accounted for by introducing a factor

$$S_A(Q^2) = \left(\frac{d\sigma}{dQ^2}\right)^{qel}_A \Big/ \left[Z\left(\frac{d\sigma}{dQ^2}\right)^{el}_p + N\left(\frac{d\sigma}{dQ^2}\right)^{el}_n\right] \qquad (6)$$

for a nucleus with Z protons and N neutrons. The quasi-elastic scattering cross section in the numerator of equation 6 was calculated using a simple Fermi - gas model [24] and checked against a shell model calculation [25]. The free proton and neutron elastic scattering cross sections in the denominator were calculated using the parameterisation of the proton form factor of Atwood [26]. For deuterium the

quasi elastic suppression factor was taken to be of the form 1 - $F_D^2(Q^2)$ [5], where F_D is the deuteron form factor.

The radiative correction was defined as the ratio $\eta(x, Q^2)$ of the single photon cross section (eq. 1) to the computed cross section which included the radiative effects. It was applied as a multiplicative factor in equation 4. Fig.6 shows the contours of fixed values of $1-\eta$ on the (x, Q^2) plane for an incident muon energy of 280 GeV. It should be noted that the restriction of the data to small values of y excludes the region where the contributions of radiative processes are large and varying rapidly.

The inaccuracies in the radiative correction factor cause a systematic error in the measured value of F_2. The sources of these inaccuracies and their magnitudes have been carefully investigated and discussed in detail in ref. 27. The total systematic error on η was obtained by adding quadratically all the inaccuracies. In our acceptance region this error is everywhere smaller than 5% and is consistent with the uncertainty quoted in the previous analyses [28].

A check on the radiative correction calculations has been made previously in a different kinematic range from this experiment [29]. A further check was made here by comparing the fractions of events which contain secondary tracks from the calcium and deuterium targets as a function of ν. Among the different radiative processes contributing to the measured cross section, only wide angle bremsstrahlung (WAB) depends on the target, neglecting a small contribution from quasielastic reactions. The WAB events should contain only the scattered muon with no other secondary tracks apart from those in which the photon converts to a positron-electron pair (41% of the events from the calcium and 14% from the deuterium targets). The ratio of the fraction of events containing no secondary track from calcium to the fraction from deuterium was observed to rise with ν up to its highest value (~200 GeV) since the WAB process becomes relatively more important at larger values of ν in calcium. The observed rise agreed with that expected from the WAB process within the errors after allowance for the conversion of photons and acceptance effects.

This gives confidence in the procedure applied to correct the data sample for events of radiative origin. A similar analysis, i.e. separation of the DIS and WAB events using their different dynamical characteristics was made in the Fermilab experiment [30], performed with a high energy muon beam and in a similar kinematic range to ours.

5. DATA SAMPLE

The muon-deuterium, the muon-carbon and the muon-calcium scattering data presented here were acquired in the three SPS running periods in 1983. The integrated beam flux was 15.9×10^9, 1.5×10^9 and 1.3×10^9 for the deuterium, carbon and calcium data respectively. The total number of triggers acquired was 730 000, 250 000 and 475 000 for the three data sets. For deuterium and carbon the

data from the different periods have been merged by taking a weighted mean in each x, Q^2 bin following the procedure described in [15].

The reduction of the deuterium event rate in the different steps of the off-line analysis, studied using part of the final D_2 sample is illustrated below.

Fraction of events ...			
i)	... from the data acquisition		100%
ii)	... with an incoming and at least one outgoing track and an interaction vertex reconstructed, after applying phase space cuts on the incoming track and with muon fulfilling the trigger conditions		39%
iii)	... with $\nu > 5$ GeV, $Q^2 > 0.05$ GeV^2		16.2%
iv)	... where the vertex position along the beam is within 0.2 m from the target		15%
v)	... remaining after selection of a subset of trigger classes (table 5)		5.3%
vi)	... remaining after final kinematical cuts:	$10 < \nu < 150$ GeV	3.7%
		$0.2 < Q^2 < 8$ GeV^2	3.6%
		$0.002 < x < 0.17$	3.4%

The phase space cuts (entry ii)) assure that the incoming track hits the target. Beam momenta in the range 255-300 GeV were accepted. The remaining cuts for ii) are discussed in section 3.5 for a different sample of events.

The ν and Q^2 cuts for entry iii) remove events with a poorly defined interaction point. The vertex position cut iv) removes events that are likely not to originate from an interaction in the target. In order to keep the systematic errors from the acceptance correction low, only data fulfilling a subset of the (A/V) trigger classes was selected (table 5). Before submitting the data to the F_2 and cross section extraction procedure, final kinematical cuts were applied vi). The low ν and low Q^2 cuts removed elastic and quasielastic scattering events. The high ν cut limited the magnitude and the uncertainty in the corrections due to radiative processes, to the trigger and reconstruction losses and the sensitivity of the results to the shape of $R(x,Q^2)$. The discrimination against muon-electron scattering and pion/kaon decay events was obtained by the x cut. This latter cut was also partially responsible for removing the largest radiative corrections. The acceptance of the apparatus with these cuts is shown in fig.7.

6. SYSTEMATIC ERRORS

We divide the sources of systematic error into two groups: those of "statistical" (s) and of "slope" (n) character. The difference between these two is that the n-type sources give errors influencing in a systematic way the functional ("slope") dependence of the measured cross section while the s-type errors change individual data points without introducing any correlations between them. For each error source the difference between the nominal and the distorted structure

function was taken as the error. The errors are summarised in table 7 for $F_2(D)$ and in table 8 for the structure function ratios.

The errors arose from the following sources:

i) Trigger efficiency (s_1, n_1)

The trigger efficiency correction was calculated using the method discussed in section 3.6. The correction is estimated to be known with an accuracy of 20% which defines the error (s_1). This error is connected to statistical fluctuations in the sample used for calculating the correction. It is equal to about 1-2% of the structure function value and decreases with x. There is an additional error (n_1) originating from the uncertainty in the choice of variables parameterising the trigger inefficiency. Different sets of variables (such as (p', y, z) and (p', θ)) were tried, the trigger efficiency correction calculated and corresponding structure functions extracted. Extreme differences between resulting structure functions were taken as a measure of the n_1 error, which amounted to about 5-10% of F_2 and was fairly independent of x and Q^2. The error n_1 is the largest of the systematic errors.

ii) Chamber inefficiencies (s_2)

This error was determined from different sets of Monte-Carlo data generated with distorted inefficiencies of the chambers which were important for the scattered muon track reconstruction (P45, P0A and P0B). By this method an upper limit on the error equal to 30% of the estimated inefficiency was obtained. The corresponding error in the structure function is of the order of 1%.

iii) Software losses (s_3, n_2)

The efficiency of the off-line analysis chain was studied with the long chain Monte-Carlo simulations. The uncertainty (s_3) of the estimated efficiency was about 30% of the uncertainty arising as a result of the limited statistics of the Monte-Carlo sample. This gave less than 1% error on the structure function (decreasing with x and increasing weakly with Q^2). In addition the analysis of the event reconstruction losses (section 3.5) indicates an error of 2.5% for $F_2(D)$, 4% for $F_2(C)$ and $F_2(Ca)$ and 1.5% for the structure function ratios (n_2). The reconstruction is the second largest error source in the experiment.

iv) Radiative corrections (n_3)

The uncertainties in the radiative corrections were dominated by the numerical inaccuracies of the method assumed for calculating η and result in an error of less than 1% on the deuterium and carbon and around 1% on calcium structure functions (decreasing with increasing x).

v) Bin centering correction (n_4)

$F_2(x,Q^2)$ was measured at the mean Q^2 and x of a bin and not at the values of Q^2 and x at the bin centre. The difference between the central and the average x value in the bin was about 1% inside and about 10% on the edges of the acceptance region. The corresponding numbers for the Q^2 bins are 2% and 10% respectively. The procedure of shifting the structure function values to the bin centres resulted in an error on F_2 which is usually smaller than 0.5%.

vi) Calibration of incident and scattered muon momenta (n_5, n_6)

As described in section 3.3 there were two sources of systematic errors coming from the momentum calibration: an absolute momentum determination error (n_5) and that connected to the relative momentum calibration of the two spectrometers (n_6). The errors were 0.4 and 0.05% of the momentum value respectively which gave less than 1% error of the structure function value in both cases. This error increases with x and decreases with Q^2.

vii) Other errors

Other sources of systematic errors have been studied and found negligible. These include the apparatus and software analysis smearing of the events (moving them from bin to bin for example) and correcting the measured yield for the interactions occurring in the target walls (section 3.7).

viii) Total systematic error

The individual errors, s_1 to s_3 and n_1 to n_6 for the $F_2(D)$ are given in table 7. For the $F_2(C)$ and $F_2(Ca)$ the relative errors are similar to those for $F_2(D)$; the only differences are the errors n_2 and n_3. The individual errors in the structure function ratios are given in table 8. Some of the errors present in the structure functions cancel totally or partially for the ratios.

When calculating the final errors, the s-type errors were added quadratically to the statistical ones to give a final statistical error while the quadratic sum of the n-errors gave a total systematic error (for structure functions they are quoted in the two last columns of tables 9 to 12). Addition in quadrature was used since the individual error sources are uncorrelated.

ix) Absolute normalisation

The uncertainty in the absolute flux is 5% due primarily to uncertainties in the dead time corrections at the first level of the SAIT processor. This uncertainty is the same for all data and cancels when taking the ratio of two data sets. In

addition cross sections obtained from deuterium and carbon in three separate experimental runs differed in normalisation by up to 3 and 6% respectively. These differences must be considered as a further systematic uncertainty which does not cancel when taking the ratio of the data sets. The data on the calcium target were taken in one run only and the normalisation error was then assumed to be equal to that of the carbon sample.

Thus the normalisation uncertainty on ratios of structure functions is 7%. The absolute normalisation uncertainty on the deuterium structure function is 7% and that on carbon and calcium is 8%.

7. RESULTS AND DISCUSSION

7.1 The Nucleon Structure Function from Deuterium

The final results for the nucleon structure function obtained from deuterium, $F_2(D)$, are presented in table 9 and figures 8 and 9 as a function of x and Q^2. Only points for which both statistical and systematic errors were smaller than 30% are included. In addition to the errors quoted in the table and marked on the figures there is an overall normalisation error of 7%. Values of the coefficients of the function fitted to the data are given in table 6.

No significant x dependence is visible in any Q^2 interval for $Q^2 < 3$ GeV^2 (fig. 8). This means that the increase of the structure function coming from the increase of the quark sea in the limit of small x implied by QCD at higher Q^2 is relatively weak at low Q^2. For larger Q^2, the data are shifted towards the higher x values due to the experimental acceptance and the x dependence observed in DIS emerges. This pattern is confirmed when comparing our results with the data coming from SLAC [5,6], CHIO [7] and previous EMC measurements in the deep inelastic region, $x > 0.03$, $Q^2 > 7$ GeV^2 [16] (fig. 10).

Fig. 11 shows the Q^2 dependence of $F_2(D)$ compared to the other experiments [5,6,7,16]. There is reasonable agreement with the SLAC data [5,6] at lower Q^2 and the previous EMC measurements at higher Q^2 [16] once systematic errors are taken into account. However, there is a tendency for the data from this experiment to rise faster with Q^2 than extrapolation to SLAC [5,6] and the previous EMC measurements [16] would suggest. This trend, which is not due to the assumed shape of $R(x,Q^2)$, is not significant within the systematic errors on the data presented here. In addition a relative normalisation correction of 8% between the data of [5,6] and [16] is necessary. The data in fig.11 are therefore consistent with a linear variation with $\log Q^2$. Since F_2 is found to be constant with x for $x < 0.1$, the values were averaged over x in this range. Fig. 12 shows the mean value of F_2 for $x < 0.1$ as a function of Q^2 on linear (12a) and logarithmic (12b) scales in Q^2. The data extrapolate to $F_2 = 0$ at $Q^2 = 0$ as expected from the conservation of the electromagnetic current. The value of F_2 seems to decrease suddenly with decreasing Q^2 for $Q^2 \leq 1$ GeV^2.

Quantitative QCD calculations of the low x, low Q^2 structure function were done recently by Gluck, Godbole and Reya (GGR) [10a] in order to make predictions for the forthcoming experiments at the HERA collider. GGR used the moments' evolution equations. The starting point for the evolution was taken as $\mu^2 = (0.25\ GeV)^2 \approx (M/3)^2$ where valence quarks are assumed to be the only partons existing in the nucleon ("static point"). The gluons and sea partons are then generated radiatively ("dynamical" structure functions) using QCD. The generated gluon and sea parton distributions grow more steeply with decreasing x than the conventionally calculated distributions [10b]. Fig.13 shows our data at x=0.005 compared to the predictions of [10a] and [10b] made for the proton structure function. The dynamical structure function of GGR [10a] overshoots the data points which extrapolate well to the conventional structure functions [10b].

At low Q^2 hadronic behaviour of a virtual photon is expected according to the vector meson dominance concept [3,4]. A theoretical scheme, incorporating both parton and VMD mechanisms independently of the value of Q^2 involved, is provided by the generalised vector meson dominance (GVMD) model. In addition to the GVMD there exist several phenomenological parameterisations extrapolating structure functions (parton model ideas) from the scaling region to low values of Q^2 [5,7,31] which, although useful, lack the dynamical content of GVMD. A model based on the GVMD representation was developed by Kwiecinski and Badelek [32] to describe the structure function results of this experiment (cf. fig.13). The formalism made it possible to extend in a dispersive way the parton model structure function onto the low Q^2 region in addition to the low mass vector meson contribution. It was shown that the magnitude of the partonic contribution to F_2 can be as high as 50% of the vector meson contribution in the low Q^2, low x region.

7.2 Nucleon Structure Functions from Carbon and Calcium

The nucleon structure function obtained from carbon, $F_2(C)$, is given in table 10 and from calcium, $F_2(Ca)$, is shown in table 11 and figures 14 and 15 as a function of x and Q^2. Values of the coefficients of the function fitted to the data are given in table 6. In figures 14 and 15 there are also data from the EMC NA2 muon-iron experiment [17] as well as the CDHSW neutrino-iron results obtained with R=0 [8]. The charged lepton structure function was computed from the CDHSW ν and $\bar{\nu}$ data neglecting the contribution of charm but making the correction for the strange quark distribution [8]. The statistical and systematic errors are added in quadrature. There is reasonable agreement between the different experiments within errors except perhaps in the lowest x bin where the CDHSW data appear to be somewhat higher than the data presented here. Unlike the deuterium data (fig.8), fig. 14 shows that F_2 from calcium tends to decrease with x indicating the onset of shadowing (see below). There is no such trend in the neutrino data which are however rather sparse in the appropriate low x region. Fig. 15 shows that a similar log Q^2 dependence exists in the calcium data to that observed for deuterium (fig.9).

7.3 Structure Function Ratios

Fig.16 shows the x dependence of the structure function ratios obtained in this experiment for $0.3 < Q^2 < 3.2$ GeV^2 (full points) and data from other high-energy charged lepton scattering experiments obtained on <A>=12, <A>=55 and <A>=120 targets. The bars represent statistical and systematic errors combined in quadrature wherever the latter were available. There is an additional error of 7% due to the uncertainty in normalisation on our points.

The results and their discussion was published before in a short communication [33]. The numerical values of the structure function ratios from our experiment are given in table 12.

Our data extrapolate smoothly to those obtained with real ($Q^2 = 0$) photons of 60 GeV [34] and join to those obtained with electrons and muons at larger x [35,36,37,38]. Together the data show a pronounced signal of shadowing which increases with nuclear atomic number. This signal, at least for <A>=55 targets, does not show any saturation even at lowest values of x (x~0.003). The data are also consistent with some antishadowing for x between 0.1 and 0.3. The cross-over point between shadowing and antishadowing shifts towards larger values of x when A increases. This is visible when comparing the $F_2(C)/F_2(D)$ and $F_2(Sn)/F_2(D)$ ratios. Fig. 17 shows the structure function ratios plotted versus Q^2 obtained for two intervals of x: $0.004<x<0.018$ and $0.018 <x<0.110$. No significant Q^2 dependence is observed, the increase with x of the mean value of the ratio visible for calcium being a reflection of the strong x dependence in $F_2(Ca)/F_2(D)$.

Attempts were made to describe shadowing by both VMD and parton (QCD) mechanisms [3,4,39]. In the VMD models one assumes that it is predominantly the hadronic component of the photon which interacts with the target. At sufficiently high photon energies this component may travel a distance exceeding the nuclear diameter, $2R_A$. A virtual photon will then interact with the nucleus like an ordinary hadron. In the rest frame of the nucleus the propagation distance for a photon being in the hadronic state of mass M_h is

$$\Delta d \sim \frac{1}{\Delta E} = \frac{2\nu}{Q^2 + M_h^2} \quad . \tag{7}$$

Here ΔE is the energy difference between the energy, ν, of the virtual photon and E_h of the hadron of the same momentum. In the VMD picture, the condition for the onset of shadowing is that $\Delta d > 2r$ (assuming that the h-N cross section is large enough), where r is the distance between two neighbouring hadrons in the nucleus, equal to about 1 fm. From formula 7 it is easy to see that the shadowing of a particular hadronic state M_h will disappear when ν is small and Q^2 is large. The last condition corresponds to $Q^2 >> M_h^2$ since M_h^2 is equal to 0.5-1 GeV^2 for the ρ, ω and ϕ mesons. When $Q^2 >> M_h^2$ then $\Delta d \sim 1/Mx$ and the condition for the

onset of shadowing is expressed in terms of the Bjorken scaling variable only: $x < x_A = 1/2Mr \approx 0.1$.

The shadowing signal observed in this experiment is most pronounced when the data are plotted as a function of x. No clear Q^2 dependence is observed in fixed x intervals (cf. fig.17), which also implies a lack of ν dependence in these intervals. This suggests that the vector meson dominance model, at least in its simplest form, is not the main explanation of the shadowing observed in our data.

An alternative explanation of shadowing is offered by the parton model valid in the high Q^2 region. The model is formulated in the reference frame where the nucleus moves with infinite momentum. In this frame the Lorentz contraction makes partons fuse, i.e. overlap spatially and interact (e.g. by recombination), thus reducing the effective parton density (per nucleon). The interaction of partons belonging to different nucleons begins when the longitudinal size of a parton having a certain momentum fraction x exceeds the Lorentz contracted longitudinal size of the nucleon. This leads to the supression of the parton density for values of x smaller than a certain value x_A (shadowing) and (possibly) to the enhancement of the parton distributions at $x>x_A$ (antishadowing), i.e. to a redistribution of the parton momenta. The value of x_A is the same as that obtained in the laboratory frame, $x_A = 1/2Mr \approx 0.1$. The physical basis of the parton fusion approach is the assumption that at sufficiently small x, the constituent partons (quarks and/or gluons) in a nucleus are not independent as is assumed in the parton model, that is the cross section for hard scattering will not grow linearly with A.

Recent calculations, based on QCD [39,40] lead to shadowing which decreases slowly with Q^2 for $Q^2 \to \infty$ at fixed x while for fixed Q^2 it should increase with decreasing x. They also predict a weak increase with A of the x value of the cross-over point, once surface effects in the nucleus are included [40b]. Both predictions are compatible with the data. It is interesting to note that according to the parton fusion model used in ref. 41 antishadowing should reach its maximum at $x_0 = m_\pi / m_N = 0.15$; full shadowing is expected at $x_c < x_0 A^{-1/3}$ (=0.044 for A=40). This last prediction is not confirmed by the data of fig. 16.

Inspired by our data, Kwiecinski and Badelek [42] developed a model for the nuclear shadowing of virtual photons in which both the VMD and partonic mechanisms were considered. A shadowing correction to the parton distributions in a nucleus is then given in terms of the Pomeron structure function, i.e. in terms of the quantities measured in the deep inelastic diffractive production on a nucleon. The results of the model calculations are shown by the solid line in fig.16. At the Q^2 values measured in this experiment the dominant contribution to shadowing comes from the rescattering of vector mesons. The partonic mechanism, however, gives a significant contribution, especially at $x<0.01$ and is essential for obtaining the "scaling" of the shadowing signal.

A partonic model of shadowing was proposed by Castorina and Donnachie [43]. Their calculations (dashed line in fig. 16) are based on the assumption similar to that in [42], that the small x limit of the nucleon structure function is controlled by Pomeron exchange. In a nuclear environment the coupling of the Pomeron to a quark is suppressed. This suppression is the result of nucleon overlap which induces a depletion of the sea and gluon distribution and demonstrates itself as shadowing.

In this context it is interesting to note that indications of shadowing have been observed in the comparison of neutrino and antineutrino scattering from neon and deuterium targets. The observed depletion of the charged current cross section per nucleon in neon seen at very low Q^2 (<1 GeV^2), low x (<0.2) and low ν vanishes rapidly with Q^2. This has been interpreted as due to geometric shadowing of the weak propagator, $W^{\pm}$ [44]. For shadowing to occur, the virtual $W^{\pm}$ boson must fluctuate into a virtual hadron system analogous to VMD for photons.

8. SUMMARY

Results have been presented on the measurement of the cross section for the small angle scattering of 280 GeV positive muons by deuterium, carbon and calcium targets. A dedicated trigger system designed specifically for the purpose of this experiment allowed the recording of events with scattering angles down to 2 mrad.

Structure functions $F_2(x,Q^2)$ for free and bound nucleons were extracted for $0.002<x<0.17$ and $0.2<Q^2<8$ GeV^2. The free nucleon structure function F_2 obtained from deuterium does not display any significant x dependence, as expected by Regge theory. The Q^2 dependence of this structure function is linear in $\log Q^2$, i.e. the same as at higher four momentum transfers. This behaviour emerges even more clearly when comparing with the data from other experiments taken both at higher and similar values of the kinematical variables, Q^2 and x. The measured F_2 extrapolates well to the values calculated from conventional parton distributions [10b] but disagrees with those calculated from dynamically generated parton distributions [10a].

The structure functions of nucleons bound in calcium and carbon show a significant x dependence as compared to deuterium which is interpreted as a shadowing effect. The position of the cross-over point shifts towards larger values of x with increasing nuclear atomic mass. The shadowing becomes more pronounced with increasing A and there are indications of antishadowing for $0.1<x<0.3$.

The structure function ratios do not show any significant Q^2 dependence for fixed x intervals. This suggests that shadowing may be due to partonic interactions as well as a vector meson structure of the virtual exchange photon.

Quantitative models developed in connection with our data contain contributions from both partonic and Vector Meson Dominance mechanisms.

Our data are consistent with those obtained from other charged lepton scattering experiments, both at similar and higher values of x and Q^2 as well as with those obtained in photoproduction. The present data add valuable information on the low x behaviour of the $F_2(A)/F_2(D)$ ratio for the light, $<A>=12$, and medium size, $<A>=55$, nuclei. This ratio has been measured extensively for x values above 0.1 ("the EMC effect"). The compilation of the world data for the $<A>=55$ nuclei is presented in fig. 18. A consistent experimental picture of the ratios of structure functions for bound and free nucleons emerges over a wide range of x.

Acknowledgements

We wish to thank many people at our home institutes and at CERN for support to this experiment. In particular, we thank A.Davies, R.Dobinson and E.Watson for their help with the small-angle trigger. In addition, we thank the SPS division for providing us with the muons and the DD and EP divisions for helping us with the FASTBUS pilot project. Finally the financial support from agencies in home countries and from CERN is gratefuly acknowledged.

REFERENCES

1. M.Breidenbach et al., Phys. Rev. Lett. 23 (1969) 935.
2. R.Windmolders, Proc. Int. XXIV Conf. on High Energy Phys., Munich, 1988, eds. R.Kotthaus and J.H.Kühn, Springer-Verlag, 1989.
3. G.Grammer and J.D.Sullivan, in Electromagnetic Interactions of Hadrons, eds A.Donnachie and G.Shaw, Plenum Press, 1978.
4. T.H. Bauer et al., Rev.Mod.Phys. 50 (1978) 261 and references therein.
5. SLAC, E61; S.Stein et al., Phys.Rev. D12 (1975) 1884.

6a. SLAC, E49a; J.S.Poucher et al., Phys. Rev. Lett. 32 (1974) 118 and SLAC-PUB-1309 (Dec. 1973).

b. SLAC-MIT, E87; A. Bodek et al., Phys.Rev. D20 (1979) 1471.
SLAC-MIT, E87; A. Bodek et al., Phys.Rev.Lett. 50 (1983) 1431

7. CHIO, B.A.Gordon et al., Phys.Rev. D20 (1979) 2645.
8. CDHSW, B.Vallage, Thèse de l'Université Paris XI, Orsay, 1986 and P. Berge et al.,"A Measurement of Differential Cross-Sections and Nucleon Structure Functions in Charged-Current Neutrino Interactions on Iron", to be published
9. BEBC, D. Allasia et al., Z. Phys. C28 (1985) 321.
BEBC, K.Varvell et al., Z.Phys. C36 (1987) 1.
BEBC, J.Guy et al., Z.Phys. C36 (1987) 337.

10a. M. Glück, R.M. Godbole and E. Reya, Univ. of Dortmund, preprint no. DO-TH 88/18 and Z.Phys. C41 (1989) 667.

b. M. Diemoz et al., Z.Phys. C39 (1988) 21

11. EMC, NA2; O.C.Allkofer et al., Nucl.Instr.Meth. 179 (1981) 445.
12. EMC, NA9; J.P.Albanese et al., Nucl.Instr.Meth. 212 (1983) 111.
13. A.Arvidson et al., Nucl.Instr.Meth. A251 (1986) 437.
L.Gustafsson and E.Hagberg, Nucl.Instr. Meth. A265 (1988) 521.
14. A.Arvidson et al., Uppsala Univ. preprint no. GWI-PH 7/86.
15. EMC, NA2; J.J.Aubert et al., Nucl.Phys. B259 (1985) 189.
16. EMC, NA2; J.J.Aubert et al., Nucl.Phys. B293 (1987) 740.
17. EMC, NA2; J.J.Aubert et al., Nucl.Phys. B272 (1986) 158.
18. H.Wind, Nucl.Instr. Meth. 115 (1974) 431.
19. G.Ingelman et al., Phys.Rep. 97 (1983) 31.
20. SLAC, E140; S.Dasu et al., Phys.Rev.Lett. 60 (1988) 2591.
21a. Y.S.Tsai, SLAC-PUB-848 (1971).
b. L.W.Mo and Y.S.Tsai, Rev.Mod.Phys. 41 (1969) 205.
22. I. Sick, Nucl.Phys. A218 (1974) 509.
23. I. Sick et al., Phys.Lett. B88 (1979) 245.
24. E.J. Moniz, Phys.Rev. 184 (1969) 1154.
25. J. Bernabeu, Nucl.Phys. B49 (1972) 186.
26. W.B. Atwood, SLAC-185 (1975).
27. A.Arvidson et al., Uppsala Univ. preprint no. ISV-PH 2/87.
28. T.Sloan, G.Smadja and R.Voss, Phys.Rep. 162 (1988) 45.
29. EMC, NA2, J.J.Aubert et al., Z.Phys. C10 (1981) 101, C22 (1984) 341.
30. FNAL, M.S.Goodman et al., Phys.Rev.Lett. 47 (1981) 293.
31. A. Donnachie and P.V. Landshoff, Nucl.Phys. B244 (1984) 322.
32. J. Kwiecinski and B. Badelek, Z.Phys. C43 (1989) 251.
33. EMC, NA28, M.Arneodo et al., Phys.Lett. B211 (1988) 493.
34. D.O. Caldwell et al., Phys.Rev.Lett. 42 (1979) 553 and references therein.
35. EMC, NA2', J.Ashman et al., Phys.Lett. B202 (1988) 603.
36. SLAC, E139, R.G.Arnold et al., Phys.Rev.Lett. 52 (1984) 727 and
SLAC-PUB-3257 (1983).
37. BCDMS, G. Bari et al., Phys.Lett. B163 (1985) 282.
38. BCDMS, A.C. Benvenuti et al., Phys.Lett. B189 (1987) 483.
39. L.Frankfurt and M.Strikman, Phys.Rep. 160 (1988) 235.
40a. A.H. Müller and J. Qiu, Nucl. Phys. B268 (1986) 427.
J. Qiu, Nucl. Phys. B291 (1987) 746.
b. E.L. Berger and J. Qiu, Phys.Lett. 206 (1988) 141.
41. N.N.Nikolaev and V.I.Zakharov, Phys.Lett. B55 (1975) 397.
42. J. Kwiecinski and B. Badelek, Phys.Lett. B208 (1988) 508.
43. P.Castorina and A.Donnachie, Phys.Lett. B215.(1988) 589.
44. P.P.Allport et al., Proc. Int. XXIV Conf. on High Energy Phys., Munich,
1988, eds. R.Kotthaus and J.H.Kühn, Springer-Verlag, 1989.

Table 1

Main parameters of the scintillation counters used for the small angle trigger.
For the definition of the coordinate system see chapter 2.
Angle α is measured with respect to the y axis in the yz plane.

Detector module	Element orientation	No of elements	Element dimensions (cm×cm)	Total area (cm×cm)	Thickness (mm)	Overlap (mm)
S	-	3	10 × 10	10 × 10	6	-
BHA	y, z, α (30°),	60	12 × 0.22	12 × 12	4	0.2
	y, z	20	8 × 0.4	8 × 8	4	0.0
BHB	y, z, α (30°)	60	12 × 0.22	12 × 12	4	0.2
	y, z	20	8 × 0.4	8 × 8	4	0.0
BHC	yz (2-dim.)	144	1.45 × 1.45	16.8 × 16.8	5	0.5
BHD	y	15	50 × 1.5	48.4 × 50	10	1.0
BHE	y	26	50 × 1.4	63.0 × 50	10	2.0
BHF	z	26	50 × 1.4	50 × 63.8	10	2.0

Table 2

Main parameters of the multiwire proportional chambers used for the small angle scattering. For the definition of the coordinate system see chapter 2.

Detector module	Wire orientation	Wire spacing (mm)	Chamber diameter (cm)
P0C	α (-30°), α (-30°), y, y, z, z, α (30°), α (30°)	1.0	14.4
P0A	α (-30°), z, z, y, y, α (30°)	1.0	14.4
P0B	α (-30°), z, z, y, y, α (30°)	1.0	14.4
P45	y, α (60°), y, α (-60°) y, α (60°), y, α (-60°)	2.02	90.5

Table 3

Parameters for the targets used in the small angle experiment.

Target	A	Density (g/cm^2)	Thickness (radiation length)	(nucl. coll. length)	(cm)
Deuterium	2	16.5	0.131	0.361	100
Carbon	12	37.23	0.872	0.618	20
Calcium	40.1	23.87	1.40	0.3*	15.2

*Estimated

Table 4

SAIT rates per one valid track (for definitions see section 2.4) in parts per million for the calcium and empty targets. Seven different accept/veto combinations are shown. The four-letter sequence in the first column defines the hit pattern in the hodoscope blocks BHC-BHF. The letter A means A=1 V=0 (see section 2.4), the letter V means A=0 V=1 and 0 means A=0 V=0 in the particular hodoscope block (cf. table 4). The window sizes are given in number of hodoscope elements.

Window size:	BHC = 4x4 BHD = 5	BHE = 5 BHF = 5
Notation	Calcium	Target empty
Total rate	48	16
A A A A	5.3	1.2
0 A A A	2.9	.58
A A A V	14	5.6
0 A A V	2.4	1.1
A V V A	9.8	2.5
0 V V A	.43	.080
0 0 0 0	1.8	1.3

Table 5

The finally selected subset of the SAIT combinations.
Given is the hit pattern in the hodoscope blocks BHC-BHF.
The notation is defined in table 4, the letter B means A=1, V=1.

BHC		BHD		BHE		BHF		Notation
A	V	A	V	A	V	A	V	
1	0	1	0	1	0	1	0	(AAAA)
1	0	1	0	1	0	0	0	(AAA0)
1	0	1	0	0	0	1	0	(AA 0A)
1	0	0	0	1	0	1	0	(A 0AA)
0	0	1	0	1	0	1	0	(0AAA)
1	1	1	0	1	0	1	0	(BAAA)
1	0	1	1	1	0	1	0	(ABAA)
1	0	1	0	1	1	1	0	(AABA)
0	0	1	0	1	1	1	0	(0ABA)
0	0	1	1	1	0	1	0	(0BAA)
1	0	0	1	1	0	1	0	(AVAA)

Table 6

Coefficients in the formula

$$F_2(x,Q^2) = c_{10}\{F_2^{sc} + (1 + F_2^{scb})\},$$

$$F_2^{sc} = c_1 x^{c2}(1-x)^{c3} + c_4(1-x)^{c5}, \qquad F_2^{scb} = \{c_6(1-x)^{c7} + c_8\}\ln(Q^2/c_9)$$

parametrising the nucleon structure function, $F_2(A)$, obtained from deuterium, carbon and calcium:

c_1=2.5168, c_3=3.7465, c_5=10., c_6=0.2967, c_7=7.1760, c_8=-0.0767.

The fitted coefficients are listed below.

Coefficient	Value for deuterium	Value for carbon	Value for calcium
c_2	0.7742	0.7528	0.4845
c_4	0.5223	0.4702	0.3105
c_9	5.3240 GeV^2	6.8720 GeV^2	3.2605 GeV^2
c_{10}	0.7018	0.7234	0.6389

Table 7

Values of the individual systematic errors (in %) on $F_2(D)$. See section 6 for the definition of symbols.

x	Q^2 (GeV^2)	s_1	s_2	s_3	n_1	n_2	n_3	n_4	n_5	n_6
0.0025	0.25	3.6	1.2	0.4	15	2.5	0.6	1.5	0.3	0.2
0.0025	0.35	4.0	1.5	0.6	13	2.5	0.7	0.3	0.3	0.1
0.0025	0.50	4.1	1.3	1.0	13	2.5	0.7	0.3	0.3	0.1
0.0025	0.70	4.3	1.1	1.5	11	2.5	0.8	0.9	0.4	0.0
0.0035	0.35	2.7	1.5	0.4	15	2.5	0.6	0.3	0.3	0.2
0.0035	0.50	3.4	1.2	0.6	6	2.5	0.6	0.5	0.4	0.1
0.0035	0.70	3.6	1.4	1.0	7	2.5	0.7	0.3	0.4	0.1
0.0035	0.90	3.8	1.1	1.4	11	2.5	0.8	0.2	0.4	0.0
0.0050	0.35	2.3	1.2	0.2	7	2.5	0.5	0.7	0.4	0.3
0.0050	0.50	2.4	1.1	0.4	7	2.5	0.6	0.1	0.4	0.2
0.0050	0.70	2.7	1.5	0.6	6	2.5	0.6	0.2	0.4	0.1
0.0050	0.90	3.1	1.2	0.9	6	2.5	0.6	0.3	0.4	0.1
0.0050	1.10	3.3	0.7	1.2	6	2.5	0.7	0.4	0.4	0.0
0.0050	1.40	3.4	0.9	1.5	11	2.5	0.8	0.5	0.4	0.0
0.0075	0.35	2.1	0.6	0.2	11	2.5	0.5	0.3	0.4	0.5
0.0075	0.50	1.9	1.1	0.2	7	2.5	0.5	0.5	0.4	0.3
0.0075	0.70	1.9	1.5	0.3	6	2.5	0.5	0.2	0.5	0.2
0.0075	0.90	2.1	1.3	0.5	6	2.5	0.5	0.1	0.5	0.1
0.0075	1.10	2.3	1.1	0.6	6	2.5	0.6	0.1	0.5	0.1

0.0075	1.40	2.5	0.9	0.9	7	2.5	0.6	0.5	0.5	0.1
0.0075	2.00	2.9	0.5	1.4	15	2.5	0.7	0.5	0.5	0.0
0.0105	0.35	2.0	1.0	0.2	12	2.5	0.4	0.4	0.4	0.8
0.0105	0.50	1.9	0.8	0.2	11	2.5	0.4	0.1	0.4	0.5
0.0105	0.70	1.6	1.2	0.2	6	2.5	0.4	0.1	0.5	0.4
0.0105	0.90	1.6	0.9	0.3	6	2.5	0.5	0.5	0.5	0.2
0.0105	1.10	1.7	1.3	0.4	6	2.5	0.5	0.1	0.5	0.2
0.0105	1.40	1.9	1.1	0.5	6	2.5	0.5	0.2	0.5	0.1
0.0105	2.00	2.3	1.0	0.9	6	2.5	0.6	0.2	0.5	0.1
0.0105	2.80	2.8	0.4	1.5	15	2.5	0.7	0.7	0.5	0.0
0.0150	0.35	2.2	1.1	0.1	15	2.5	0.3	0.5	0.4	1.3
0.0150	0.50	1.9	1.2	0.2	6	2.5	0.4	0.9	0.4	0.8
0.0150	0.70	1.5	1.1	0.2	5	2.5	0.4	0.5	0.5	0.6
0.0150	0.90	1.5	1.1	0.2	5	2.5	0.4	0.2	0.5	0.4
0.0150	1.10	1.3	0.7	0.3	5	2.5	0.4	0.1	0.5	0.3
0.0150	1.40	1.4	1.4	0.3	5	2.5	0.4	0.3	0.6	0.2
0.0150	2.00	1.6	1.0	0.5	5	2.5	0.5	0.2	0.6	0.1
0.0150	2.80	2.1	0.4	0.9	6	2.5	0.5	0.3	0.5	0.1
0.0150	3.60	2.5	0.3	1.3	11	2.5	0.6	0.4	0.5	0.0
0.0150	4.40	2.6	0.2	1.5	15	2.5	0.6	0.4	0.5	0.0
0.0240	0.35	2.0	1.2	0.1	9	2.5	0.3	0.6	0.4	2.2
0.0240	0.50	1.8	1.0	0.1	5	2.5	0.3	0.4	0.4	1.5
0.0240	0.70	1.6	1.0	0.2	5	2.5	0.3	0.3	0.5	1.0
0.0240	0.90	1.4	1.1	0.2	5	2.5	0.3	0.1	0.5	0.7
0.0240	1.10	1.3	1.4	0.2	5	2.5	0.3	0.4	0.6	0.6
0.0240	1.40	1.1	1.1	0.2	5	2.5	0.3	0.1	0.6	0.4
0.0240	2.00	1.1	1.1	0.3	5	2.5	0.4	0.3	0.6	0.3
0.0240	2.80	1.2	0.6	0.4	5	2.5	0.4	0.1	0.6	0.1
0.0240	3.60	1.5	0.4	0.6	6	2.5	0.4	0.2	0.6	0.1
0.0240	4.40	1.7	0.4	0.9	8	2.5	0.5	0.4	0.6	0.1
0.0240	5.60	1.9	0.2	1.2	11	2.5	0.5	0.5	0.6	0.0
0.0400	0.70	1.6	1.2	0.1	9	2.5	0.2	0.8	0.5	1.8
0.0400	0.90	1.3	1.1	0.1	6	2.5	0.2	0.3	0.6	1.3
0.0400	1.10	1.3	1.2	0.2	5	2.5	0.2	0.2	0.6	1.1
0.0400	1.40	1.0	0.9	0.2	5	2.5	0.2	0.4	0.6	0.8
0.0400	2.00	1.0	1.1	0.2	4	2.5	0.3	0.1	0.7	0.5
0.0400	2.80	0.9	0.7	0.2	4	2.5	0.3	0.2	0.7	0.3
0.0400	3.60	0.9	0.4	0.3	6	2.5	0.3	0.2	0.7	0.2
0.0400	4.40	0.9	0.4	0.4	7	2.5	0.3	0.5	0.7	0.2
0.0400	5.60	1.0	0.2	0.6	11	2.5	0.4	0.1	0.7	0.1
0.0400	7.20	1.1	0.2	0.8	20	2.5	0.4	0.2	0.7	0.1
0.0600	1.10	1.2	1.2	0.1	6	2.5	0.1	0.2	0.6	1.7
0.0600	1.40	1.1	1.3	0.1	6	2.5	0.1	0.3	0.7	1.3
0.0600	2.00	0.9	1.1	0.2	4	2.5	0.2	0.4	0.7	0.8
0.0600	2.80	0.8	0.7	0.2	4	2.5	0.2	0.1	0.7	0.5
0.0600	3.60	0.7	0.6	0.2	4	2.5	0.2	0.1	0.8	0.4
0.0600	4.40	0.7	0.5	0.3	6	2.5	0.2	0.2	0.8	0.3
0.0600	5.60	0.7	0.3	0.3	9	2.5	0.3	0.1	0.8	0.2
0.0600	7.20	0.7	0.2	0.4	15	2.5	0.3	0.1	0.8	0.1
0.0900	1.40	1.1	1.3	0.1	6	2.5	0.1	0.3	0.7	1.9

0.0900	2.00	0.9	1.0	0.1	6	2.5	0.1	0.4	0.8	1.3
0.0900	2.80	0.8	0.7	0.2	6	2.5	0.1	0.3	0.8	0.8
0.0900	3.60	0.7	0.5	0.2	6	2.5	0.1	0.1	0.8	0.6
0.0900	4.40	0.6	0.3	0.2	11	2.5	0.1	0.2	0.8	0.5
0.0900	5.60	0.6	0.3	0.2	15	2.5	0.2	0.1	0.8	0.3
0.0900	7.20	0.5	0.2	0.3	20	2.5	0.2	0.1	0.9	0.2
0.1400	2.80	0.8	0.9	0.1	4	2.5	0.4	0.9	0.9	1.3
0.1400	3.60	0.7	0.6	0.1	6	2.5	0.0	0.1	1.0	0.9
0.1400	4.40	0.6	0.4	0.2	9	2.5	0.0	0.2	1.0	0.8
0.1400	5.60	0.5	0.2	0.2	11	2.5	0.1	0.2	1.0	0.6
0.1400	7.20	0.4	0.3	0.2	15	2.5	0.1	0.2	1.0	0.4

Table 8

Contribution of individual systematic errors to the total systematic error of the structure function ratios. See section 6 for symbol definitions.

Error type	$\sigma[F_2(Ca)/F_2(D)]$	$\sigma[F_2(C)/F_2(D)]$
s_1	3%	3%
s_2	$s_2(Ca)$	$s_2(C)$
s_3	0	0
n_1	$n_1(Ca/D)$	$n_1(C/D)$
n_2	1.5%	1.5%
n_3	$\sqrt{[n_3^2(Ca) + n_3^2(D)]}$	$\sqrt{[n_3^2(C) + n_3^2(D)]}$
n_4	0	0
n_5	0	0
n_6	$\sqrt{[n_6^2(Ca) + n_6^2(D)]}$	$\sqrt{[n_6^2(C) + n_6^2(D)]}$

Table 9

The nucleon structure function, $F_2(D)$, obtained from deuterium at an incident muon energy of 280 GeV assuming $R(D) = 1.2\ (1-x)/Q^2$, as a function of x and Q^2. Symbols x and Q^2 refer to the central values of the variables in the bin. In addition to the quoted errors there is an overall normalisation error of 7%.

x	Q^2 (GeV^2)	$F_2(x,Q^2)$	Errors	
			stat.	syst.
0.0025	0.25	0.144	0.030	0.022
0.0025	0.35	0.173	0.013	0.023
0.0025	0.50	0.180	0.011	0.024
0.0025	0.70	0.225	0.028	0.026
0.0035	0.35	0.164	0.012	0.025
0.0035	0.50	0.178	0.012	0.012
0.0035	0.70	0.202	0.014	0.015
0.0035	0.90	0.235	0.024	0.027
0.0050	0.35	0.171	0.012	0.013
0.0050	0.50	0.186	0.010	0.014
0.0050	0.70	0.232	0.013	0.015
0.0050	0.90	0.233	0.014	0.015
0.0050	1.10	0.252	0.019	0.017
0.0050	1.40	0.281	0.037	0.032
0.0075	0.35	0.187	0.015	0.021
0.0075	0.50	0.193	0.010	0.014
0.0075	0.70	0.236	0.012	0.015
0.0075	0.90	0.230	0.013	0.015
0.0075	1.10	0.256	0.017	0.017
0.0075	1.40	0.272	0.016	0.020
0.0075	2.00	0.261	0.030	0.040
0.0105	0.35	0.159	0.015	0.020
0.0105	0.70	0.218	0.013	0.014
0.0105	0.90	0.248	0.016	0.016
0.0105	1.10	0.206	0.016	0.013
0.0105	1.40	0.266	0.018	0.017
0.0105	2.00	0.342	0.020	0.022
0.0105	2.80	0.343	0.043	0.052
0.0150	0.35	0.176	0.025	0.027
0.0150	0.50	0.235	0.010	0.016
0.0150	0.70	0.223	0.010	0.013
0.0150	0.90	0.240	0.013	0.014
0.0150	1.10	0.272	0.017	0.015
0.0150	1.40	0.278	0.015	0.016
0.0150	2.00	0.293	0.014	0.017
0.0150	2.80	0.378	0.024	0.025
0.0150	3.60	0.405	0.035	0.046
0.0150	4.40	0.596	0.126	0.091
0.0240	0.35	0.166	0.021	0.016

0.0240	0.50	0.230	0.011	0.013
0.0240	0.70	0.241	0.009	0.014
0.0240	0.90	0.265	0.012	0.015
0.0240	1.10	0.229	0.014	0.013
0.0240	1.40	0.272	0.013	0.015
0.0240	2.00	0.330	0.013	0.019
0.0240	2.80	0.357	0.019	0.020
0.0240	3.60	0.382	0.024	0.025
0.0240	4.40	0.383	0.031	0.032
0.0240	5.60	0.574	0.069	0.065
0.0400	0.70	0.234	0.013	0.022
0.0400	0.90	0.272	0.010	0.018
0.0400	1.10	0.295	0.012	0.017
0.0400	1.40	0.282	0.011	0.016
0.0400	2.00	0.281	0.012	0.014
0.0400	2.80	0.358	0.017	0.017
0.0400	3.60	0.425	0.023	0.028
0.0400	4.40	0.395	0.027	0.030
0.0400	5.60	0.457	0.029	0.052
0.0400	7.20	0.610	0.081	0.123
0.0600	1.10	0.296	0.016	0.020
0.0600	1.40	0.277	0.010	0.018
0.0600	2.00	0.273	0.012	0.013
0.0600	2.80	0.358	0.019	0.017
0.0600	3.60	0.369	0.025	0.018
0.0600	4.40	0.361	0.032	0.024
0.0600	5.60	0.388	0.030	0.036
0.0600	7.20	0.391	0.057	0.060
0.0900	1.40	0.281	0.027	0.019
0.0900	2.00	0.292	0.011	0.020
0.0900	2.80	0.330	0.014	0.022
0.0900	3.60	0.353	0.020	0.023
0.0900	4.40	0.386	0.027	0.044
0.0900	5.60	0.398	0.025	0.061
0.0900	7.20	0.309	0.042	0.062
0.1400	2.80	0.255	0.015	0.013
0.1400	3.60	0.329	0.018	0.022
0.1400	4.40	0.292	0.023	0.028
0.1400	5.60	0.359	0.022	0.041
0.1400	7.20	0.375	0.040	0.057

Table 10

The nucleon structure function, $F_2(C)$, obtained from carbon at an incident muon energy of 280 GeV assuming $R(C) = 1.2\ (1-x)/Q^2$, as a function of x and Q^2. Symbols x and Q^2 refer to the central values of the variable in the bin. In addition to the quoted errors there is an overall normalisation error of 8%.

x	Q^2 (GeV^2)	$F_2(x,Q^2)$	Errors	
			stat.	syst.
0.0025	0.25	0.086	0.022	0.018
0.0025	0.35	0.143	0.014	0.020
0.0025	0.50	0.141	0.011	0.019
0.0025	0.70	0.183	0.032	0.022
0.0035	0.25	0.173	0.048	0.035
0.0035	0.35	0.141	0.015	0.022
0.0035	0.50	0.163	0.015	0.012
0.0035	0.70	0.167	0.018	0.014
0.0035	0.90	0.192	0.033	0.023
0.0050	0.35	0.138	0.013	0.011
0.0050	0.50	0.171	0.013	0.014
0.0050	0.70	0.203	0.016	0.015
0.0050	0.90	0.216	0.020	0.016
0.0050	1.10	0.235	0.027	0.017
0.0050	1.40	0.197	0.047	0.023
0.0075	0.35	0.168	0.019	0.020
0.0075	0.50	0.188	0.014	0.015
0.0075	0.70	0.212	0.016	0.015
0.0075	0.90	0.193	0.018	0.014
0.0075	1.10	0.218	0.024	0.016
0.0075	1.40	0.265	0.024	0.022
0.0075	2.00	0.257	0.044	0.040
0.0105	0.35	0.181	0.027	0.020
0.0105	0.50	0.179	0.014	0.013
0.0105	0.70	0.212	0.019	0.015
0.0105	0.90	0.213	0.022	0.015
0.0105	1.10	0.279	0.033	0.020
0.0105	1.40	0.261	0.027	0.019
0.0105	2.00	0.270	0.026	0.020
0.0105	2.80	0.318	0.067	0.049
0.0150	0.35	0.195	0.020	0.030
0.0150	0.50	0.197	0.012	0.014
0.0150	0.70	0.202	0.015	0.013
0.0150	0.90	0.229	0.019	0.015
0.0150	1.10	0.245	0.024	0.016
0.0150	1.40	0.273	0.022	0.018
0.0150	2.00	0.300	0.023	0.019
0.0150	2.80	0.322	0.034	0.023
0.0150	3.60	0.388	0.064	0.046

0.0240	0.35	0.173	0.035	0.018
0.0240	0.50	0.212	0.012	0.014
0.0240	0.70	0.234	0.013	0.015
0.0240	0.90	0.227	0.015	0.015
0.0240	1.10	0.263	0.021	0.017
0.0240	1.40	0.267	0.019	0.017
0.0240	2.00	0.278	0.019	0.018
0.0240	2.80	0.262	0.024	0.017
0.0240	3.60	0.322	0.036	0.023
0.0240	4.40	0.248	0.042	0.022
0.0400	0.70	0.251	0.017	0.025
0.0400	0.90	0.251	0.015	0.018
0.0400	1.10	0.271	0.017	0.018
0.0400	1.40	0.254	0.016	0.017
0.0400	2.00	0.286	0.018	0.016
0.0400	2.80	0.297	0.026	0.017
0.0400	3.60	0.319	0.034	0.023
0.0400	4.40	0.327	0.043	0.027
0.0400	5.60	0.389	0.050	0.046
0.0600	1.10	0.275	0.028	0.020
0.0600	1.40	0.286	0.016	0.021
0.0600	2.00	0.309	0.019	0.018
0.0600	2.80	0.302	0.029	0.017
0.0600	3.60	0.373	0.043	0.021
0.0600	4.40	0.353	0.052	0.026
0.0600	5.60	0.313	0.046	0.031
0.0900	1.40	0.369	0.047	0.028
0.0900	2.00	0.303	0.017	0.022
0.0900	2.80	0.338	0.024	0.025
0.0900	3.60	0.360	0.035	0.026
0.0900	4.40	0.338	0.043	0.040
0.0900	5.60	0.297	0.038	0.046
0.0900	7.20	0.268	0.074	0.055
0.1400	2.80	0.343	0.031	0.020
0.1400	3.60	0.266	0.025	0.020
0.1400	4.40	0.368	0.041	0.037
0.1400	5.60	0.308	0.036	0.036
0.1400	7.20	0.380	0.077	0.059

Table 11

The nucleon structure function, $F_2(Ca)$, obtained from calcium at an incident muon energy of 280 GeV assuming $R(Ca) = 1.2\ (1-x)/Q^2$, as a function of x and Q^2. Symbols x and Q^2 refer to the central values of the variable in the bin. In addition to the quoted errors there is an overall normalisation error of 8%.

x	Q^2 (GeV^2))	$F_2(x,Q^2)$	Errors	
			stat.	syst.
0.0025	0.25	0.126	0.021	0.026
0.0025	0.35	0.109	0.009	0.015
0.0025	0.50	0.128	0.008	0.018
0.0025	0.70	0.134	0.019	0.016
0.0035	0.25	0.109	0.031	0.022
0.0035	0.35	0.118	0.011	0.018
0.0035	0.50	0.137	0.010	0.010
0.0035	0.70	0.125	0.011	0.010
0.0035	0.90	0.150	0.017	0.018
0.0050	0.35	0.143	0.011	0.012
0.0050	0.50	0.156	0.010	0.013
0.0050	0.70	0.164	0.011	0.012
0.0050	0.90	0.176	0.014	0.013
0.0050	1.10	0.190	0.017	0.014
0.0050	1.40	0.186	0.032	0.022
0.0075	0.35	0.153	0.012	0.018
0.0075	0.50	0.169	0.010	0.014
0.0075	0.70	0.201	0.013	0.015
0.0075	0.90	0.168	0.012	0.012
0.0075	1.10	0.187	0.015	0.014
0.0075	1.40	0.227	0.016	0.019
0.0105	0.35	0.144	0.015	0.016
0.0105	0.50	0.184	0.011	0.013
0.0105	0.70	0.185	0.014	0.013
0.0105	0.90	0.191	0.017	0.014
0.0105	1.10	0.185	0.017	0.013
0.0105	1.40	0.246	0.019	0.018
0.0105	2.00	0.245	0.018	0.018
0.0105	2.80	0.481	0.136	0.075
0.0150	0.35	0.161	0.020	0.025
0.0150	0.50	0.197	0.009	0.014
0.0150	0.70	0.192	0.011	0.012
0.0150	0.90	0.189	0.012	0.012
0.0150	1.10	0.248	0.018	0.016
0.0150	1.40	0.242	0.015	0.016
0.0150	2.00	0.246	0.014	0.016
0.0150	2.80	0.279	0.022	0.020
0.0150	3.60	0.327	0.063	0.038
0.0240	0.35	0.184	0.025	0.019

0.0240	0.50	0.213	0.010	0.014
0.0240	0.70	0.215	0.010	0.014
0.0240	0.90	0.221	0.012	0.014
0.0240	1.10	0.232	0.015	0.015
0.0240	1.40	0.260	0.015	0.017
0.0240	2.00	0.269	0.013	0.017
0.0240	2.80	0.319	0.020	0.021
0.0240	3.60	0.286	0.024	0.021
0.0240	4.40	0.360	0.039	0.032
0.0400	0.70	0.235	0.015	0.024
0.0400	0.90	0.258	0.012	0.019
0.0400	1.10	0.259	0.013	0.017
0.0400	1.40	0.284	0.013	0.018
0.0400	2.00	0.281	0.013	0.016
0.0400	2.80	0.332	0.020	0.019
0.0400	3.60	0.336	0.026	0.024
0.0400	4.40	0.354	0.032	0.029
0.0400	5.60	0.439	0.039	0.052
0.0400	7.20	0.431	0.116	0.088
0.0600	1.10	0.289	0.018	0.022
0.0600	2.00	0.320	0.014	0.018
0.0600	2.80	0.332	0.022	0.019
0.0600	3.60	0.292	0.027	0.017
0.0600	4.40	0.403	0.043	0.029
0.0600	5.60	0.375	0.038	0.037
0.0600	7.20	0.294	0.076	0.046
0.0900	1.40	0.332	0.035	0.025
0.0900	2.00	0.292	0.012	0.022
0.0900	2.80	0.311	0.017	0.023
0.0900	3.60	0.327	0.024	0.024
0.0900	4.40	0.325	0.031	0.038
0.0900	5.60	0.292	0.027	0.045
0.0900	7.20	0.410	0.063	0.084
0.1400	2.80	0.326	0.023	0.019
0.1400	3.60	0.324	0.023	0.024
0.1400	4.40	0.310	0.027	0.031
0.1400	5.60	0.412	0.031	0.048
0.1400	7.20	0.332	0.053	0.052

Table 12

Ratios of the carbon and calcium cross sections relative to those of deuterium. In addition to the quoted errors there is an overall normalisation error of 7%.

Q^2 range (GeV^2)	$<Q^2>$ (GeV^2)	x	$\sigma(C)/\sigma(D)$	$\sigma(Ca)/\sigma(D)$	Errors	
					stat.	syst.
0.3 - 3.2	0.51	0.0035	0.86		0.06	0.05
	0.66	0.0050	0.87		0.04	0.04
	0.79	0.0075	0.90		0.04	0.04
	0.97	0.0105	0.92		0.04	0.04
	1.08	0.015	0.90		0.03	0.04
	1.10	0.024	0.90		0.03	0.04
	1.46	0.04	0.92		0.03	0.05
	1.73	0.06	1.02		0.04	0.05
	2.29	0.09	1.03		0.05	0.05
	0.52	0.0035		0.71	0.04	0.06
	0.66	0.0050		0.77	0.03	0.06
	0.79	0.0075		0.80	0.03	0.05
	0.96	0.0105		0.82	0.03	0.05
	1.10	0.015		0.83	0.02	0.04
	1.16	0.024		0.88	0.02	0.04
	1.49	0.04		0.95	0.03	0.05
	1.71	0.06		1.08	0.04	0.05
	2.29	0.09		0.98	0.04	0.05

x range	<x>	Q^2 (GeV^2)	$\sigma(C)/\sigma(D)$	$\sigma(Ca)/\sigma(D)$	Errors	
					stat.	syst.
0.004 - 0.11	0.011	0.35	0.94		0.06	0.05
	0.017	0.50	0.90		0.03	0.05
	0.016	0.70	0.93		0.03	0.05
	0.026	0.90	0.90		0.03	0.05
	0.031	1.10	0.97		0.04	0.04
	0.038	1.40	0.97		0.03	0.05
	0.052	2.00	0.99		0.03	0.04
	0.055	2.80	0.87		0.04	0.04
	0.056	3.60	0.89		0.05	0.04
	0.058	4.40	0.83		0.07	0.04
	0.064	5.60	0.79		0.07	0.04
	0.009	0.35		0.85	0.05	0.06
	0.017	0.50		0.87	0.03	0.04
	0.016	0.70		0.84	0.03	0.05
	0.026	0.90		0.83	0.03	0.04
	0.035	1.10		0.89	0.03	0.04
	0.038	1.40		0.98	0.03	0.04
	0.052	2.00		0.94	0.02	0.05
	0.053	2.80		0.90	0.03	0.06
	0.056	3.60		0.81	0.04	0.05
	0.055	4.40		0.93	0.06	0.05
	0.063	5.60		0.86	0.06	0.05

Figure captions

1. The Feynman diagram for the first order deep inelastic muon-nucleon scattering process.

2. Layout of the EMC NA28 experiment (top view). The first spectrometer magnet, the VSM, contains the target (marked is the position of the solid target) and a streamer chamber. The second spectrometer magnet, the FSM, contains multiwire proportional chambers. V means veto counter, BH means scintillator hodoscope measuring in the beam region, H means hodoscope used by the large angle trigger, P means multi-wire proportional chamber and W means drift chamber. Hodoscopes and chambers essential for the small angle measurements are described in tables 1 and 2 and marked with a box. Dimensions in y are not to scale.

3. Principle of operation of the Small Angle Interaction Trigger (SAIT).

4. Distributions of the longitudinal coordinates of the interaction points in deuterium and calcium targets (continuous curve). The same distributions obtained with the deuterium target vessel empty and for the calcium target removed are also shown (broken line). No kinematic cuts were applied. Marked are the positions of the counters surrounding the targets.

5. Reconstructed minus generated vertex x coordinate for a muon scattering angle of 2.5 mrad (a) and 6.5 mrad (b) for the simulated data. The energy transfer ν was equal to 70 GeV. The curves are least squares fits of Gaussian distributions.

6. Fraction of events of radiative origin, $1-\eta$, on the (x,Q^2) plane for the deuterium (a) and calcium (b) targets in the kinematical region of this experiment.

7. Acceptance of the apparatus on the (x,Q^2) plane. Lines denote kinematical cuts.

8. The nucleon structure function, $F_2(D)$ obtained from deuterium as a function of x for different intervals of Q^2 (values in GeV^2). Statistical errors are indicated by bars; systematic are shown by the band beneath. In addition to the marked errors there is an overall normalisation error of 7%.

9. The nucleon structure function, $F_2(D)$ obtained from deuterium as a function of Q^2 for different intervals of x. Errors as in fig.8.

10. $F_2(D)$ as a function of x for different intervals of Q^2 compared to the results of the experiments of CHIO [7], SLAC [6a] and SLAC-MIT [6b]. Errors are statistical.

11. $F_2(D)$ as a function of Q^2 for different intervals of x compared to the results of the experiments of EMC [16], CHIO [7], SLAC [6a] and SLAC-MIT [6b]. Errors are statistical.

12. Mean value of $F_2(D)$ for $x < 0.1$ as a function of Q^2 on linear (a) and logarithmic (b) scales in Q^2. Error bars represent statistical and systematic errors summed in quadrature.

13. $F_2(D)$ as a function of Q^2 at x=0.005 from this experiment, compared to the proton structure function F_2^p predicted from the dynamical [10a] and conventional [10b] parton distributions and to $F_2(D)$ from the GVMD calculations [32]. Error bars represent statistical and systematic errors summed in quadrature.

14. The nucleon structure function, $F_2(Ca)$ obtained from calcium as a function of x for different intervals of Q^2 compared to the results of experiments of CDHSW [8] and EMC [17] both obtained with iron and evaluated with R=0. Error bars represent statistical and systematic errors summed in quadrature. In addition there is an overall normalisation error of 8%.

15. $F_2(Ca)$ as a function of Q^2 for different intervals of x. Errors as in fig.14.

16. Structure function ratios, $F_2(A)/F_2(D)$, obtained in this experiment for the range $0.3<Q^2<3.2$ GeV^2 (full circles) compared with other leptoproduction experiments on different targets: the former EMC results for carbon, copper and tin (Ashman et al. [35], open circles), Arnold et al. [36], Bari et al. [37], Benvenuti et al. [38], Stein et al. [5], Goodman et al. [30]. The crosses marked on the vertical axis are ratios from a photoproduction experiment, Caldwell et al. [34], where the energy of the photon beam was 60 GeV. Error bars represent statistical and systematic errors summed in quadrature except the SLAC data [5, 36] where only statistical errors are given. The x values of the points obtained in the Fermilab experiment at 209 GeV [30] were computed by dividing the published Q^2 values by $2M\nu$ using ν = 150 GeV, which is the average value for their acceptance region ($110 < \nu < 200$ GeV for $Q^2 < 3$ GeV^2 and $40 < \nu < 200$ GeV for $Q^2 > 3$ GeV^2). The lines are predictions of models of ref.42 (solid) and of ref.43 (dashed).

17. Structure function ratios versus Q^2 obtained for two intervals of x: $0.004<x<0.018$ (closed points) and $0.018<x<0.110$ (open points). Error bars give statistical and systematic errors summed in quadrature.

18. Compilation of the data on the nuclear to nucleon structure function ratio (the "EMC effect") for the $<A>=55$ nuclei [5,6b,30,34,35,36,38]. Data coming from the EMC experiments are marked by closed points. The errors are statistical.

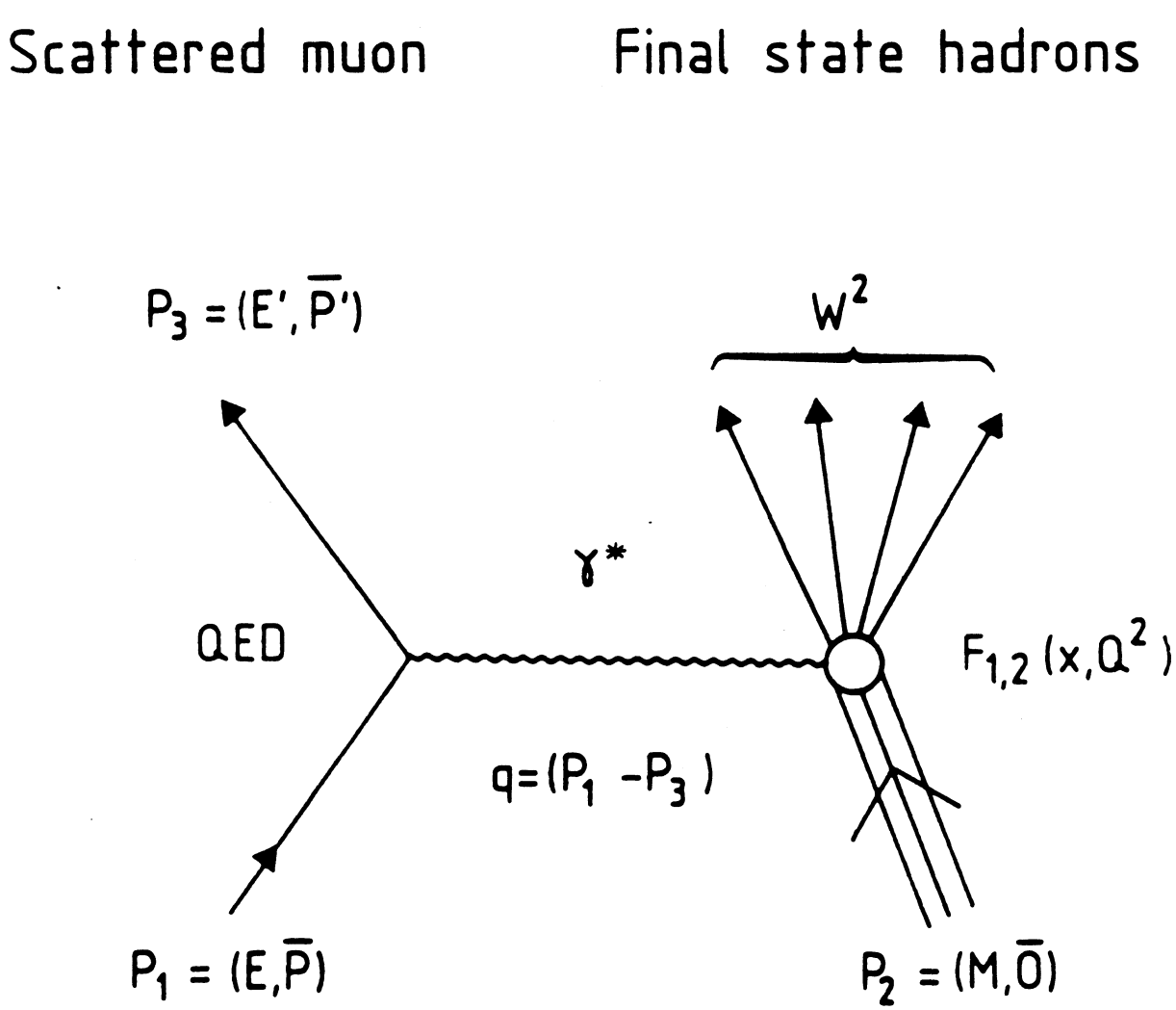
Scattered muon
Final state hadrons
$P_3 = (E', \bar{P}')$
W^2
γ^*
QED
$F_{1,2}(x, Q^2)$
$q = (P_1 - P_3)$
$P_1 = (E, \bar{P})$
$P_2 = (M, \bar{0})$
Incident muon
Target nucleon

Fig. 1

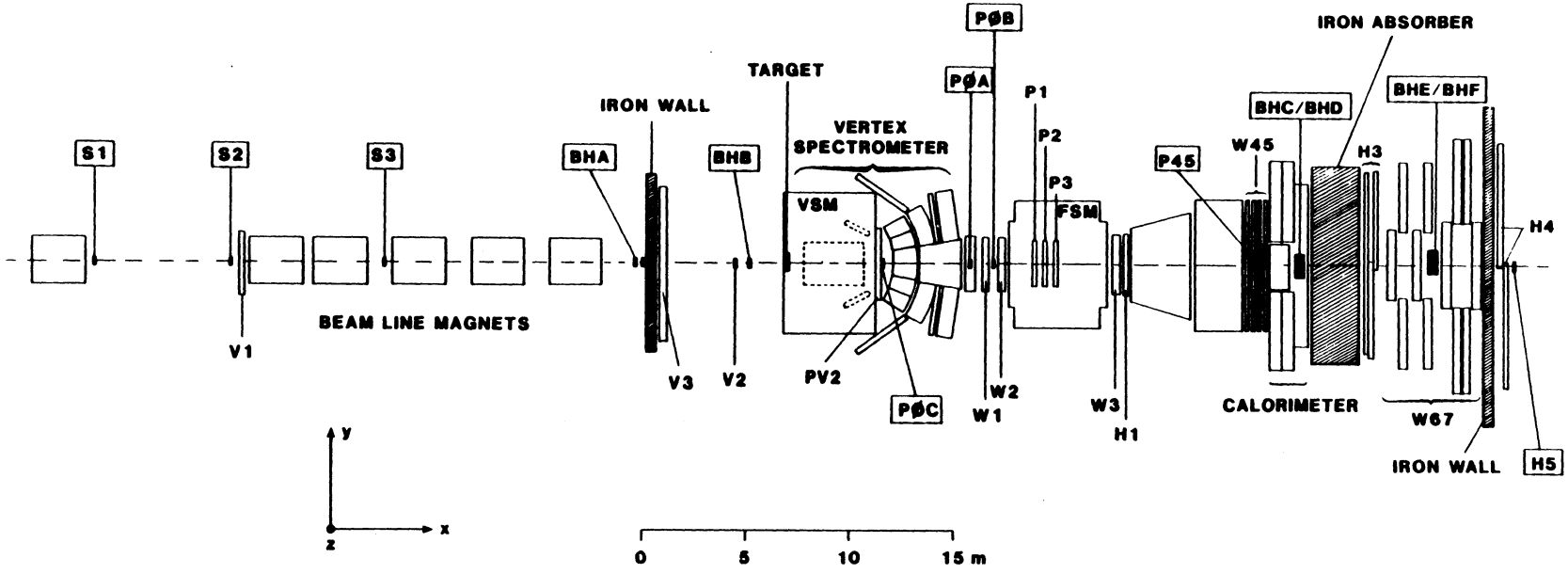
S1
S2
S3
BHA
BHB
IRON WALL
TARGET
VERTEX
SPECTROMETER
VSM
PØB
PØA
P1
P2
P3
FSM
P45
W45
BHC/BHD
IRON ABSORBER
H3
BHE/BHF
H4
BEAM LINE MAGNETS
V1
V3
V2
PV2
PØC
W2
W1
W3
H1
CALORIMETER
W67
IRON WALL
H5
y
x
z
0
5
10
15 m

Fig. 2

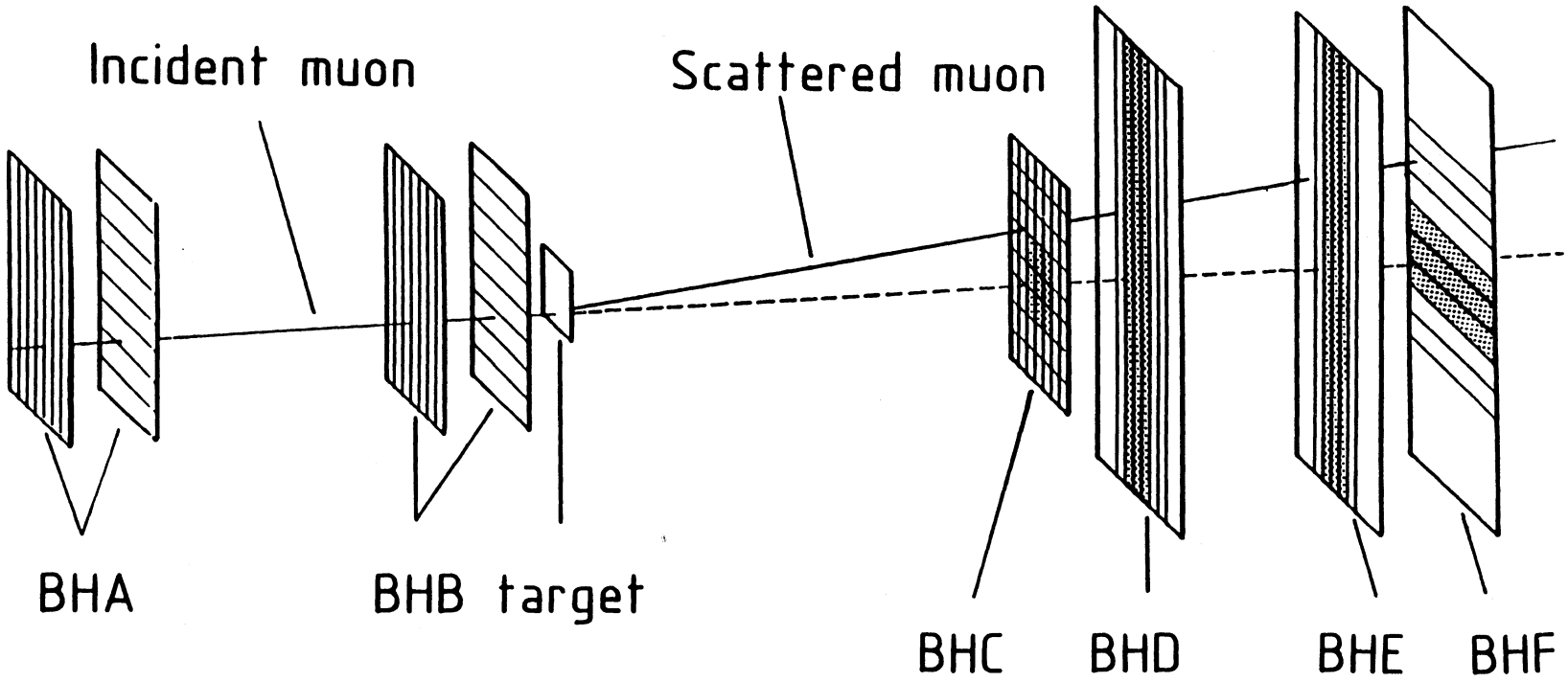

Fig. 3

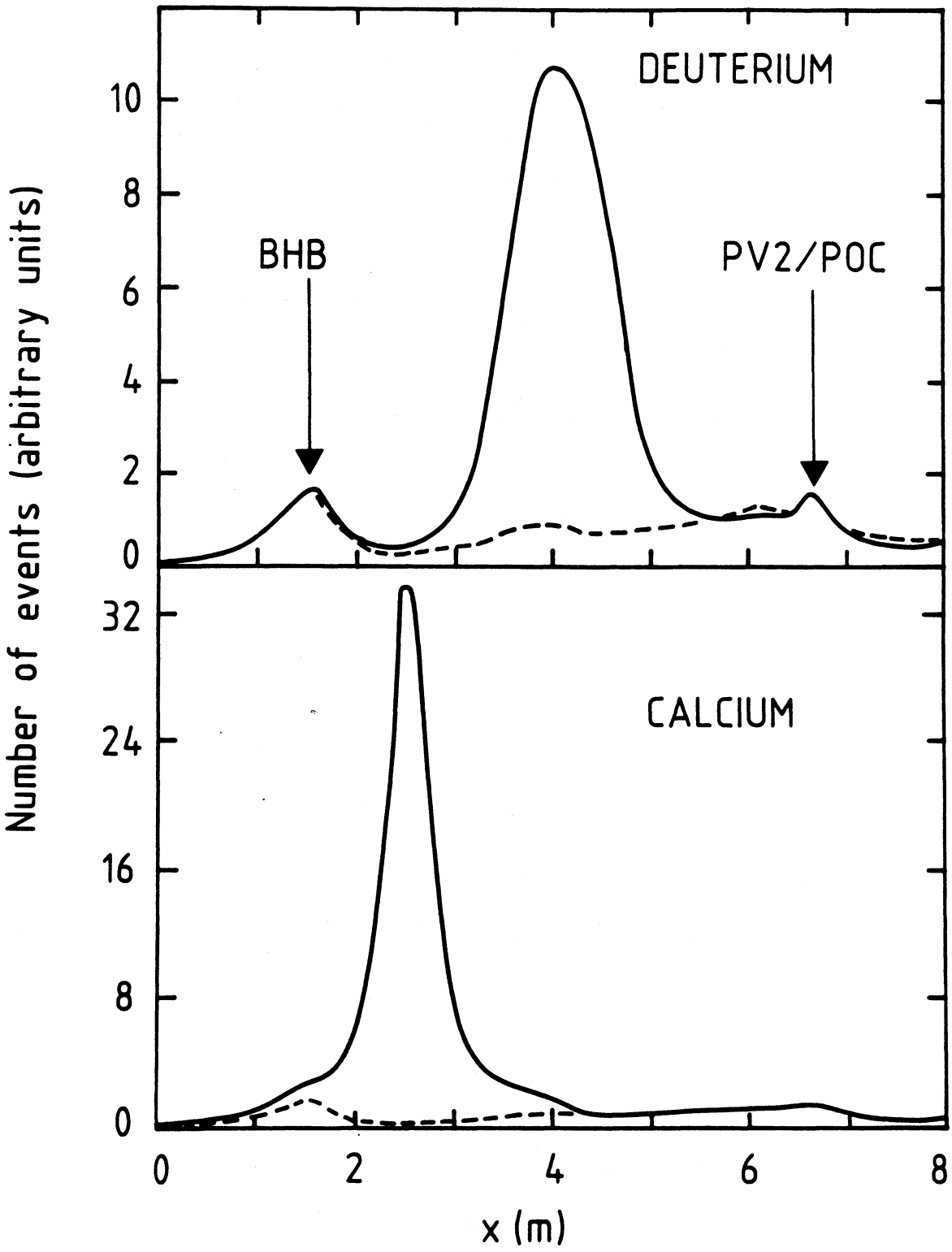
DEUTERIUM
BHB
PV2/POC
CALCIUM
Number of events (arbitrary units)
x (m)
0
2
4
6
8
10
16
24
32

Fig. 4

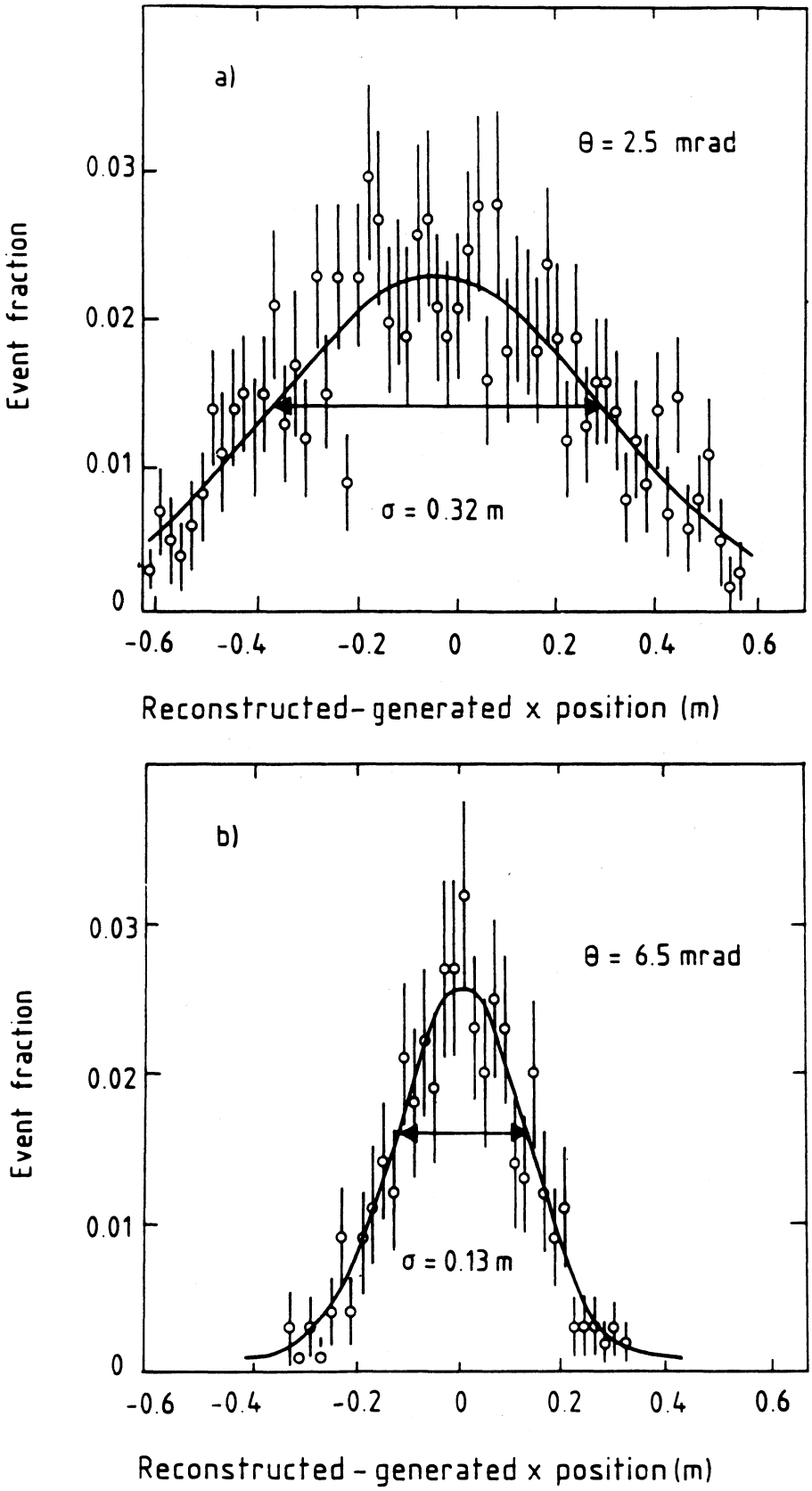
a)
θ = 2.5 mrad
σ = 0.32 m
Event fraction
0.03
0.02
0.01
0
-0.6
-0.4
-0.2
0
0.2
0.4
0.6
Reconstructed-generated x position (m)
b)
θ = 6.5 mrad
σ = 0.13 m
Event fraction
0.03
0.02
0.01
0
-0.6
-0.4
-0.2
0
0.2
0.4
0.6
Reconstructed - generated x position (m)

Fig. 5

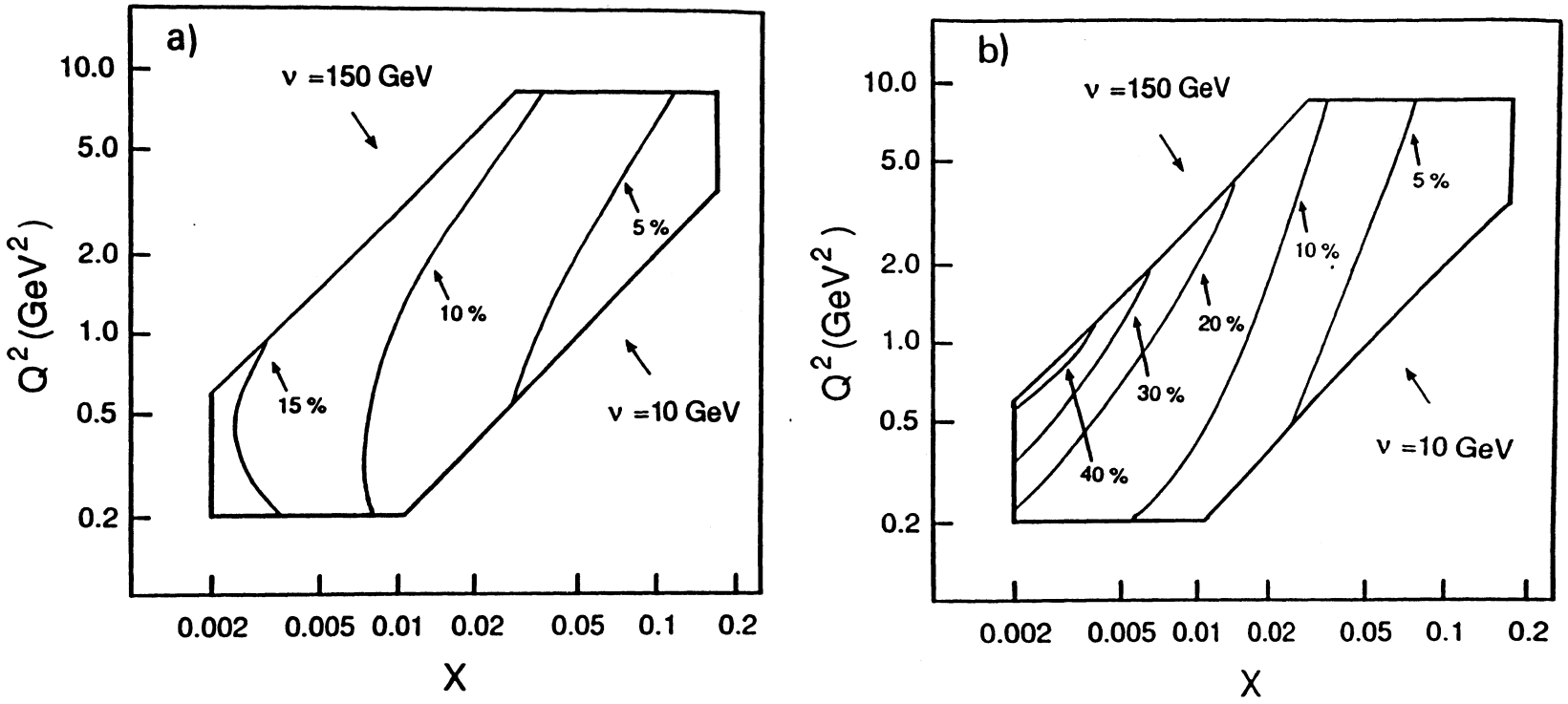
a)
ν =150 GeV
ν =10 GeV
15 %
10 %
5 %
10.0
5.0
2.0
1.0
0.5
0.2
Q²(GeV²)
0.002
0.005
0.01
0.02
0.05
0.1
0.2
X
b)
ν =150 GeV
ν =10 GeV
40 %
30 %
20 %
10 %
5 %
10.0
5.0
2.0
1.0
0.5
0.2
Q²(GeV²)
0.002
0.005
0.01
0.02
0.05
0.1
0.2
X

Fig. 6

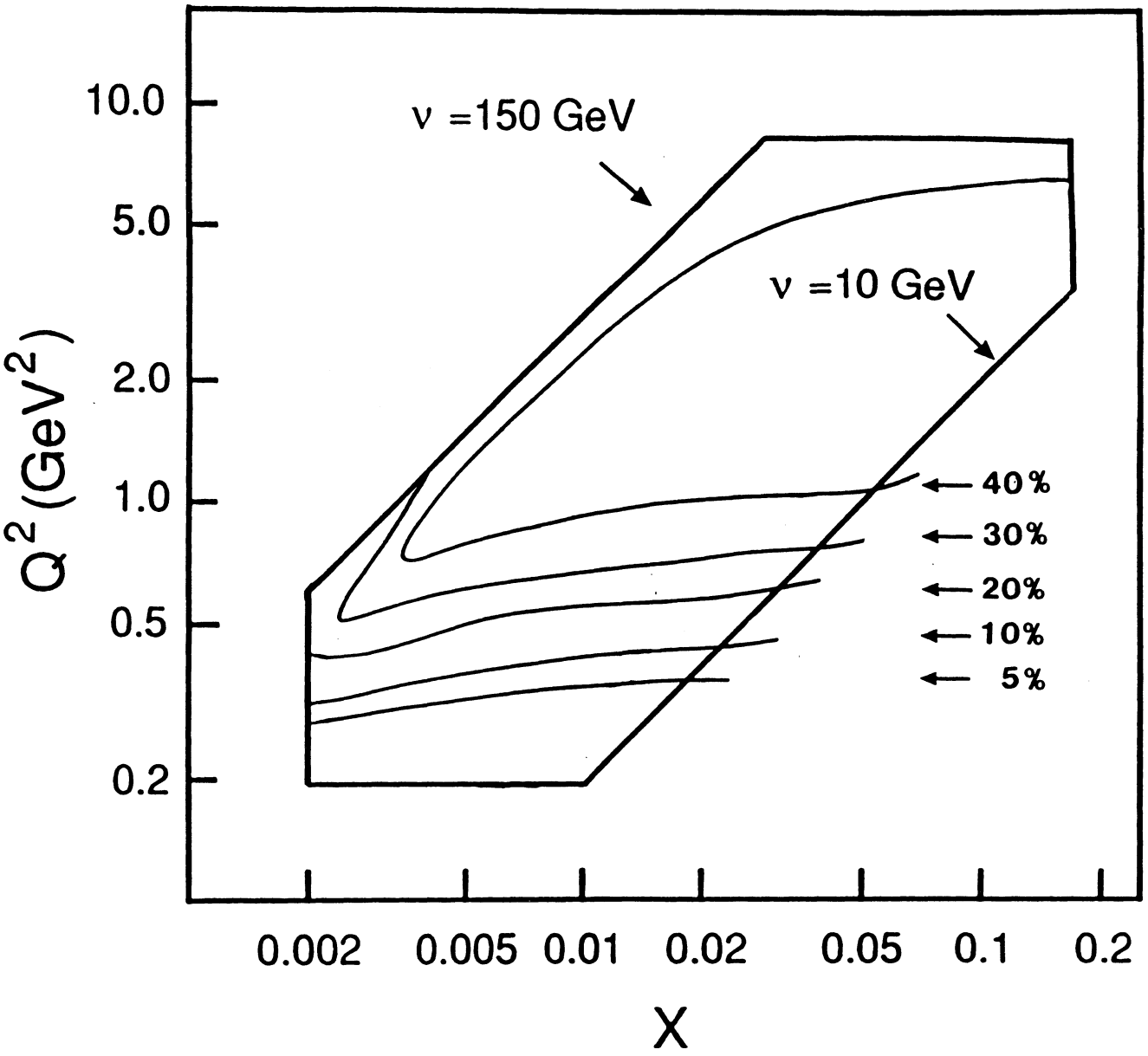
10.0
5.0
2.0
1.0
0.5
0.2
Q^2 (GeV^2)
ν =150 GeV
ν =10 GeV
40%
30%
20%
10%
5%
0.002
0.005
0.01
0.02
0.05
0.1
0.2
X

Fig. 7

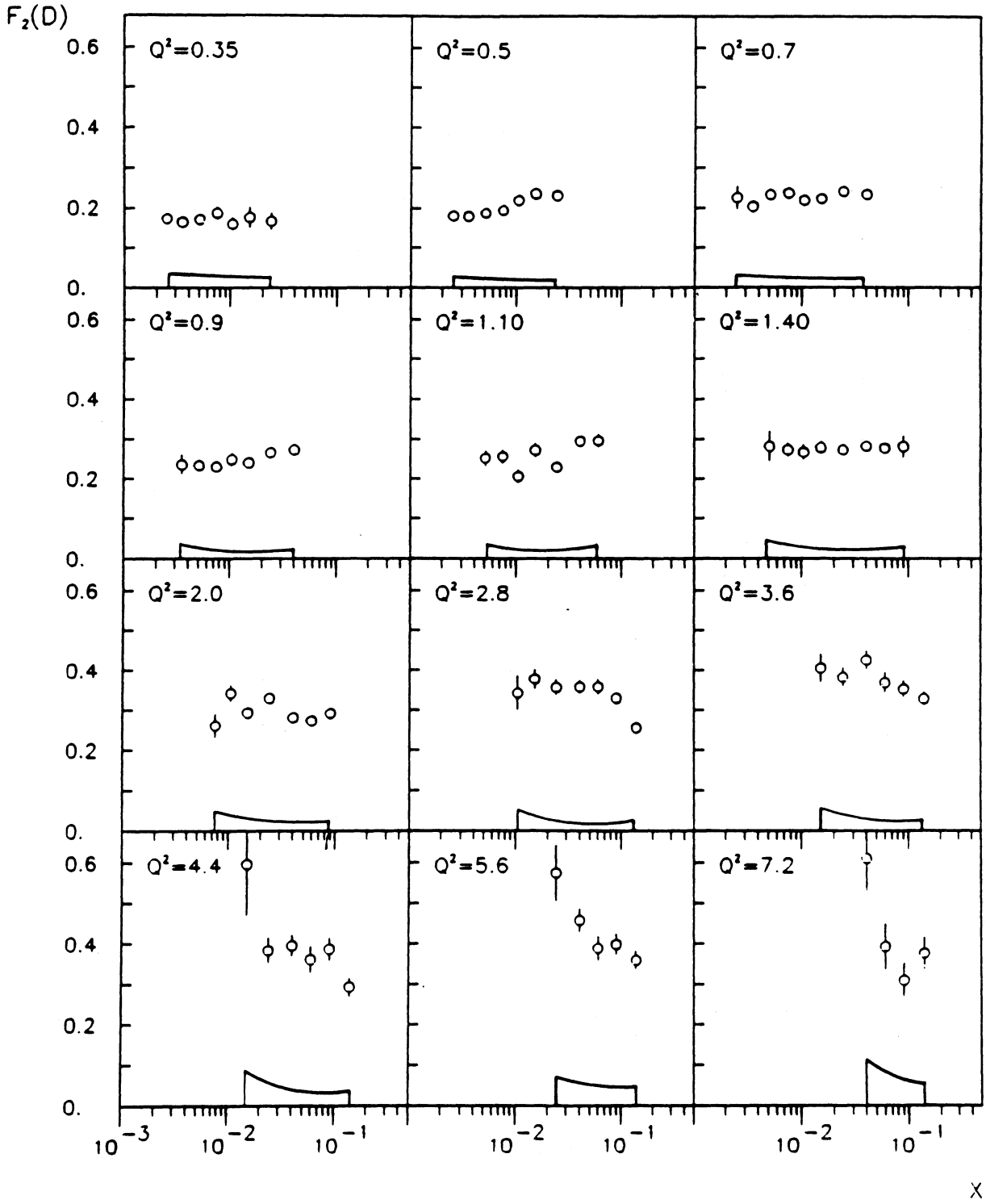
$F_2(D)$
Q^2=0.35
Q^2=0.5
Q^2=0.7
Q^2=0.9
Q^2=1.10
Q^2=1.40
Q^2=2.0
Q^2=2.8
Q^2=3.6
Q^2=4.4
Q^2=5.6
Q^2=7.2
0.6
0.4
0.2
0.
10^{-3}
10^{-2}
10^{-1}
X

Fig. 8

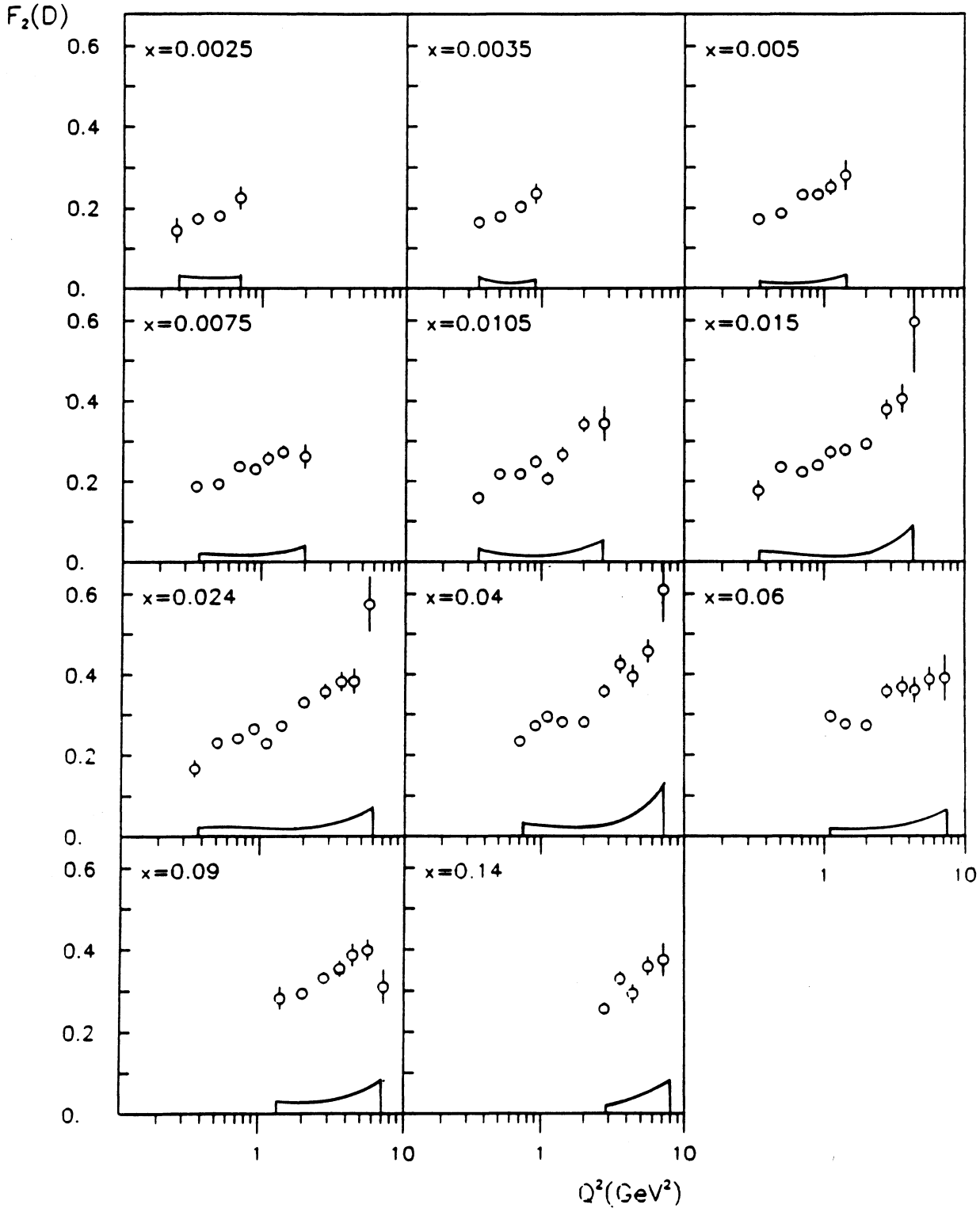
$F_2(D)$
x=0.0025
x=0.0035
x=0.005
x=0.0075
x=0.0105
x=0.015
x=0.024
x=0.04
x=0.06
x=0.09
x=0.14
0.6
0.4
0.2
0.
1
10
$Q^2(GeV^2)$

Fig. 9

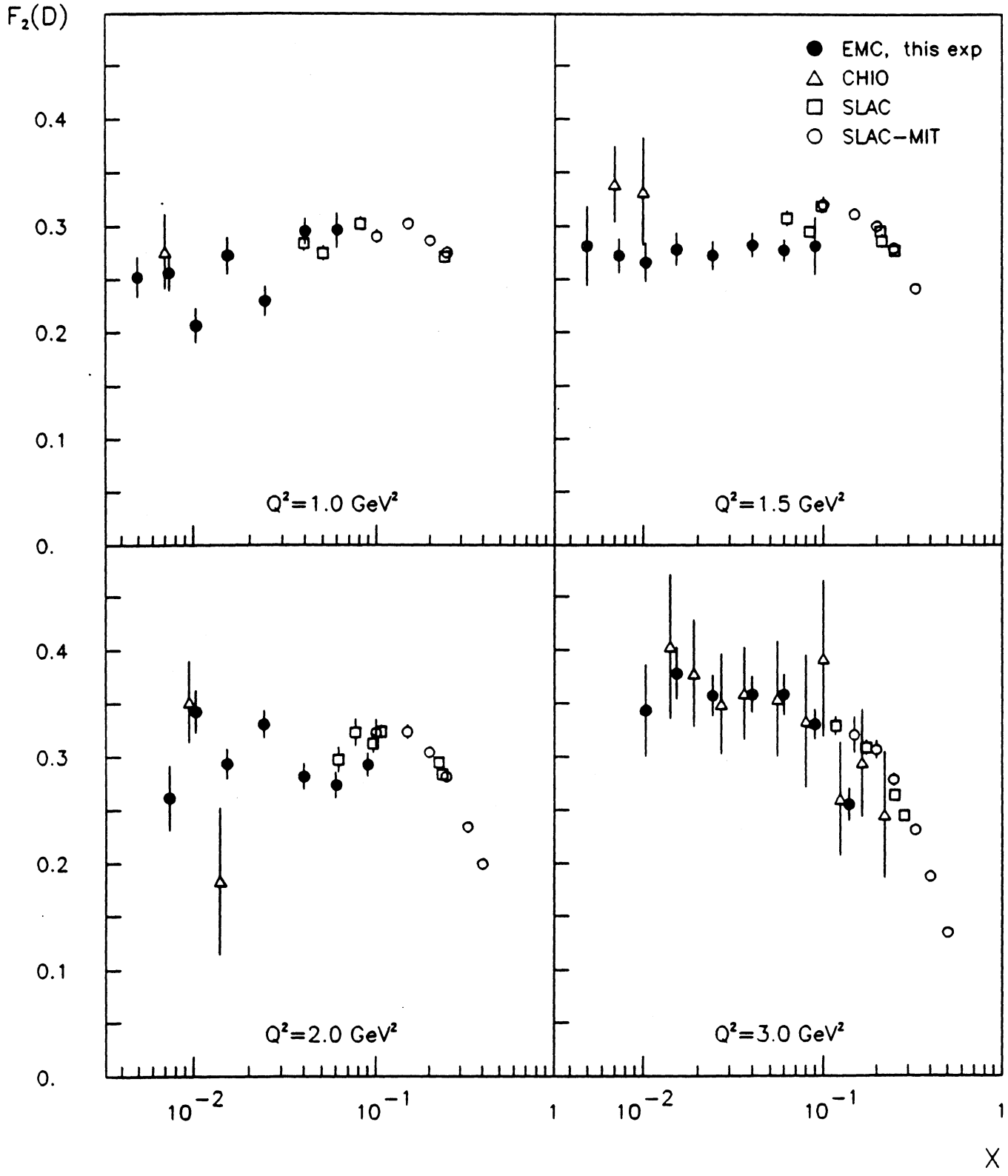
$F_2(D)$
EMC, this exp
CHIO
SLAC
SLAC–MIT
Q^2=1.0 GeV^2
Q^2=1.5 GeV^2
Q^2=2.0 GeV^2
Q^2=3.0 GeV^2
0.
0.1
0.2
0.3
0.4
10^{-2}
10^{-1}
1
X

Fig. 10

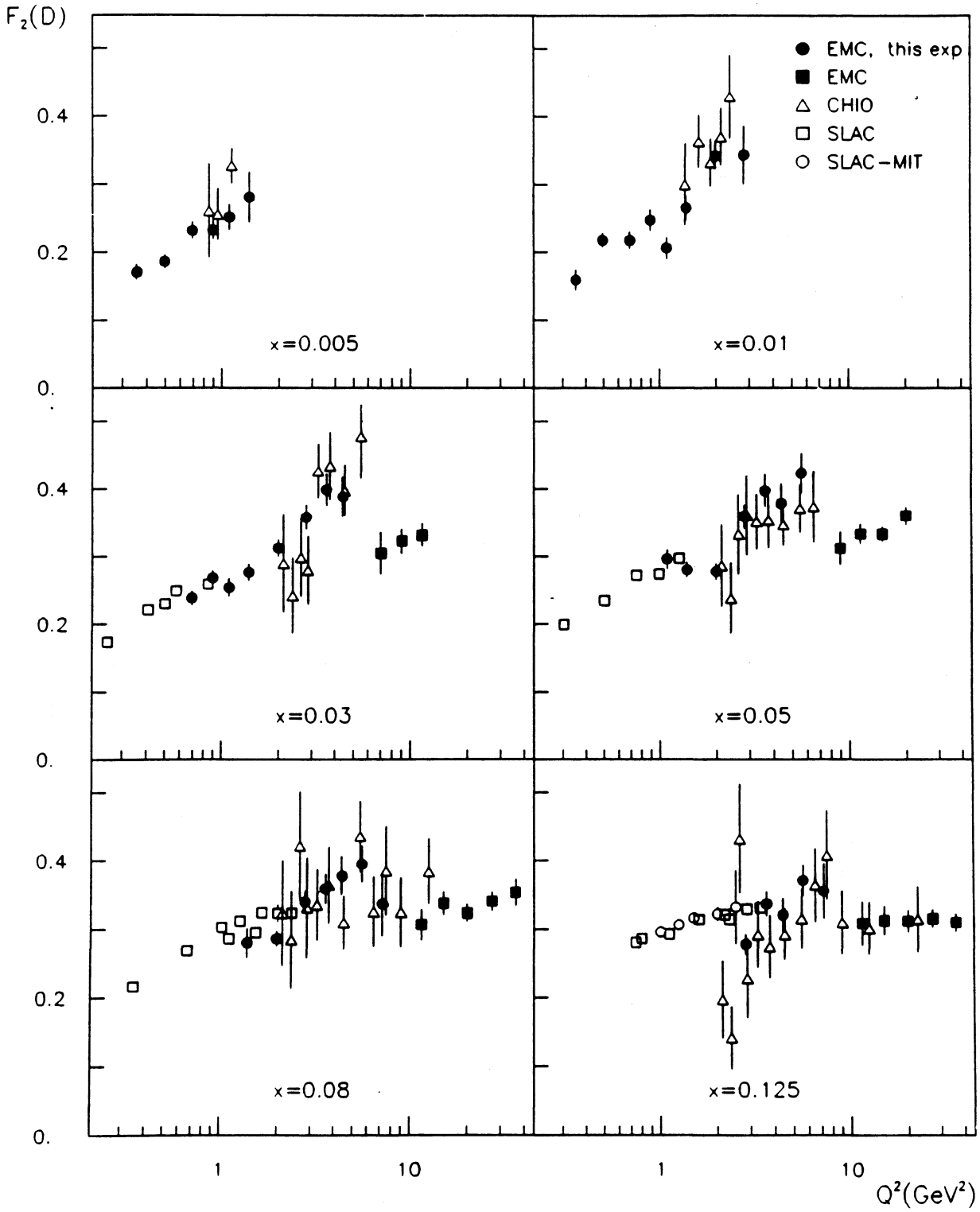
$F_2(D)$
EMC, this exp
EMC
CHIO
SLAC
SLAC-MIT
x=0.005
x=0.01
x=0.03
x=0.05
x=0.08
x=0.125
0.
0.2
0.4
1
10
$Q^2(GeV^2)$

Fig. 11

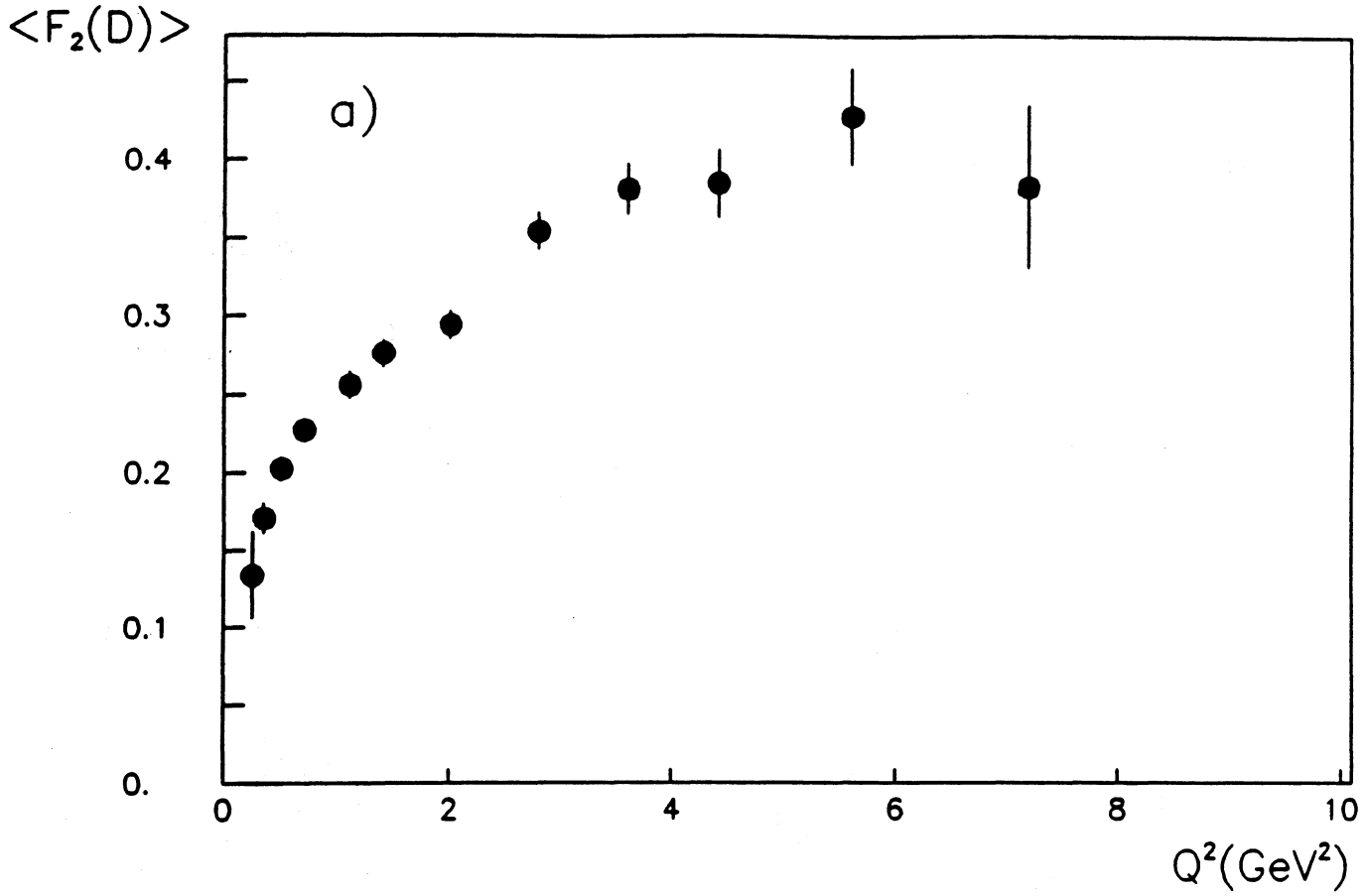
<F₂(D)>
a)
0.4
0.3
0.2
0.1
0.
0
2
4
6
8
10
Q²(GeV²)

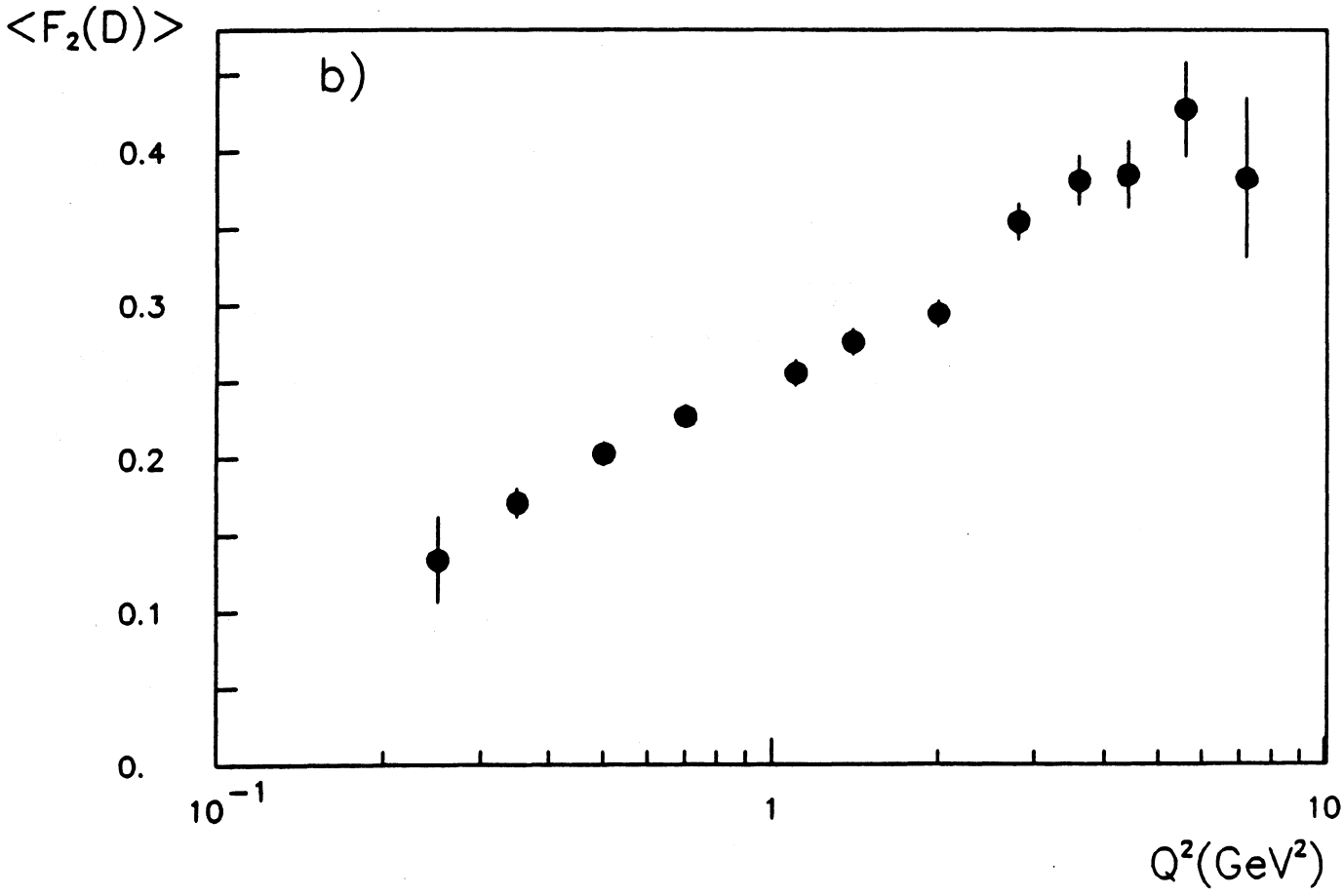
<F₂(D)>
b)
0.4
0.3
0.2
0.1
0.
10⁻¹
1
10
Q²(GeV²)

Fig. 12

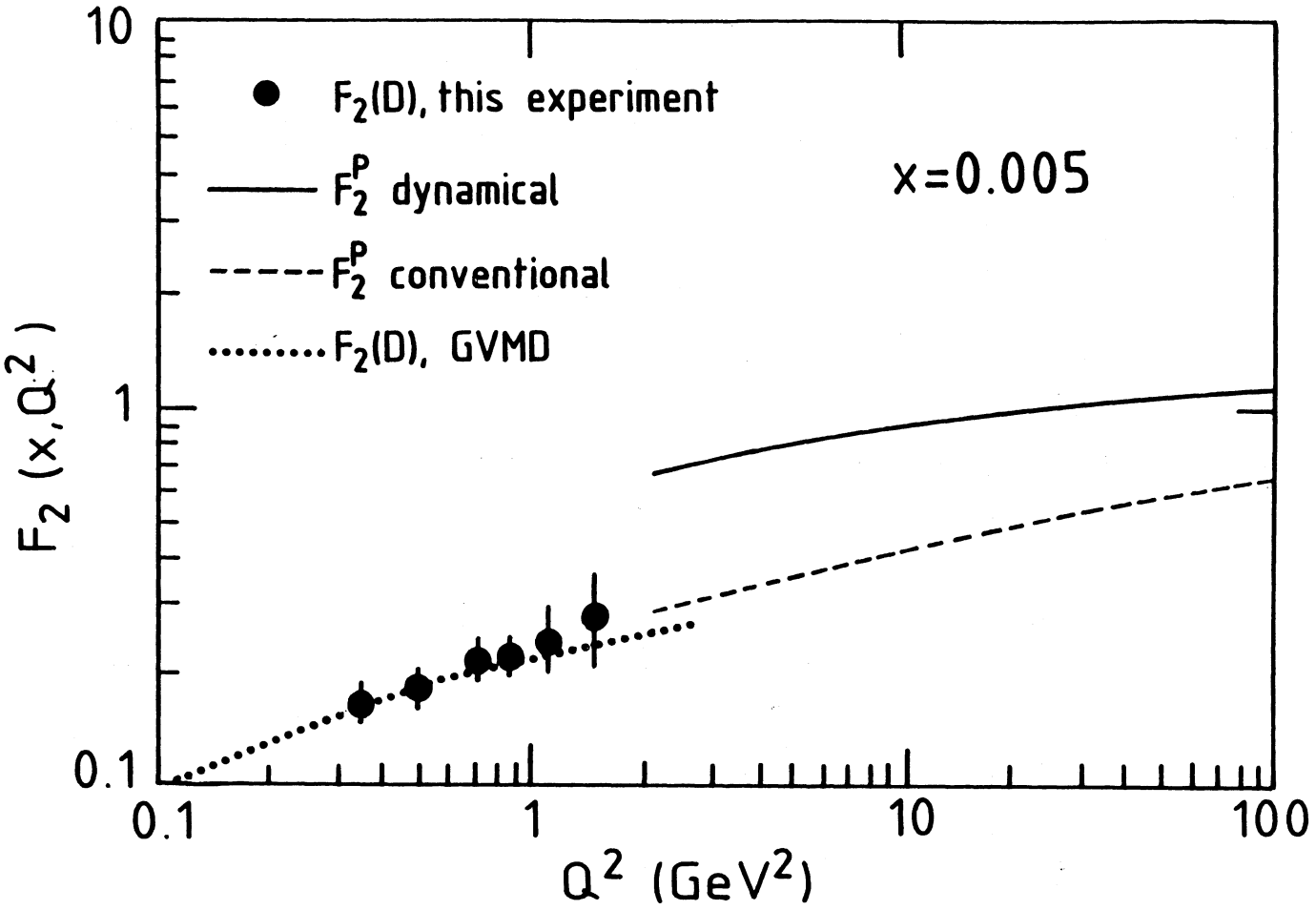
10
1
0.1
0.1
1
10
100
$F_2(x,Q^2)$
Q^2 (GeV^2)
F_2(D), this experiment
F_2^P dynamical
F_2^P conventional
F_2(D), GVMD
x=0.005

Fig. 13

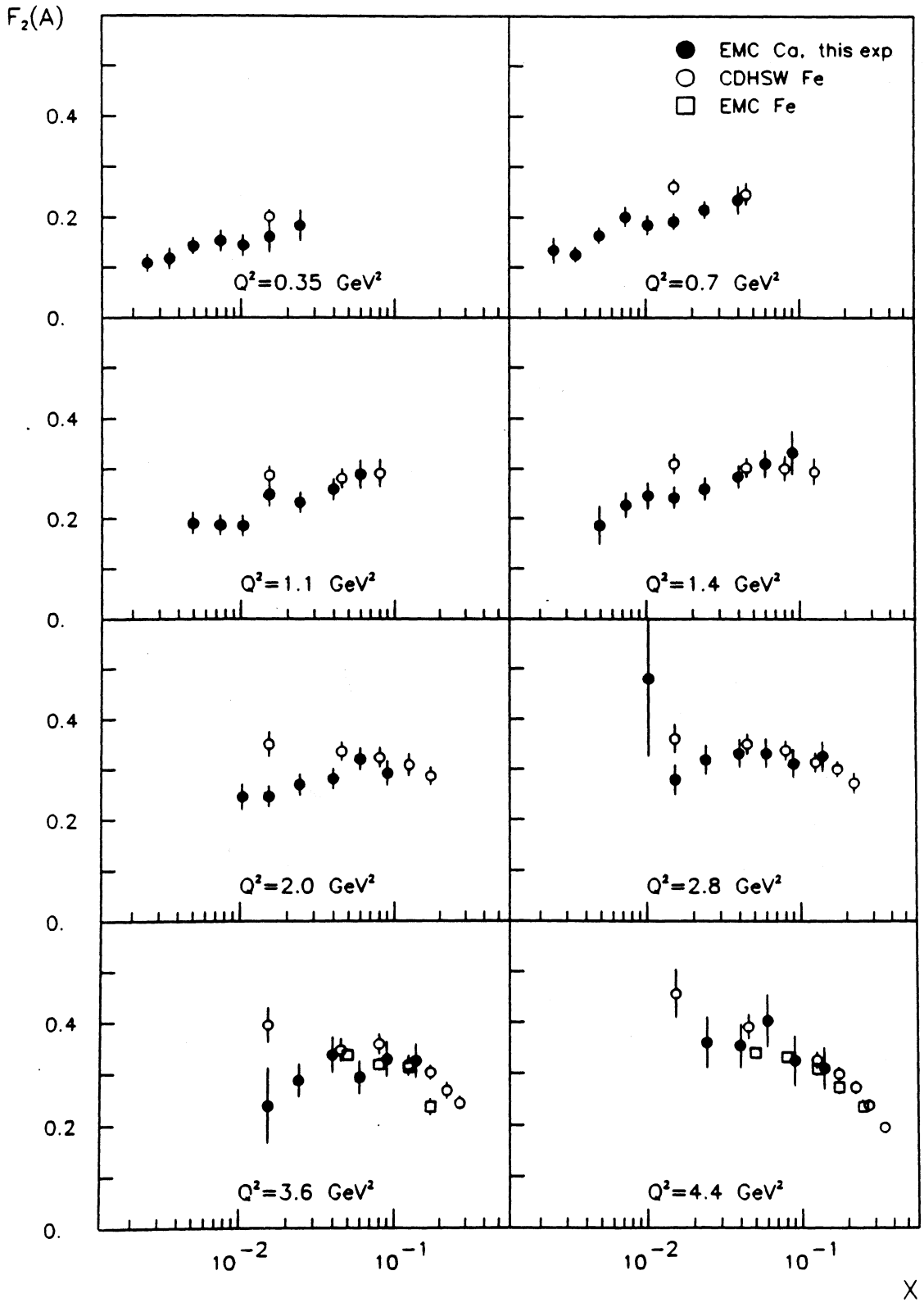
$F_2(A)$
EMC Ca, this exp
CDHSW Fe
EMC Fe
Q^2=0.35 GeV^2
Q^2=0.7 GeV^2
Q^2=1.1 GeV^2
Q^2=1.4 GeV^2
Q^2=2.0 GeV^2
Q^2=2.8 GeV^2
Q^2=3.6 GeV^2
Q^2=4.4 GeV^2
0.
0.2
0.4
10^{-2}
10^{-1}
X

Fig. 14

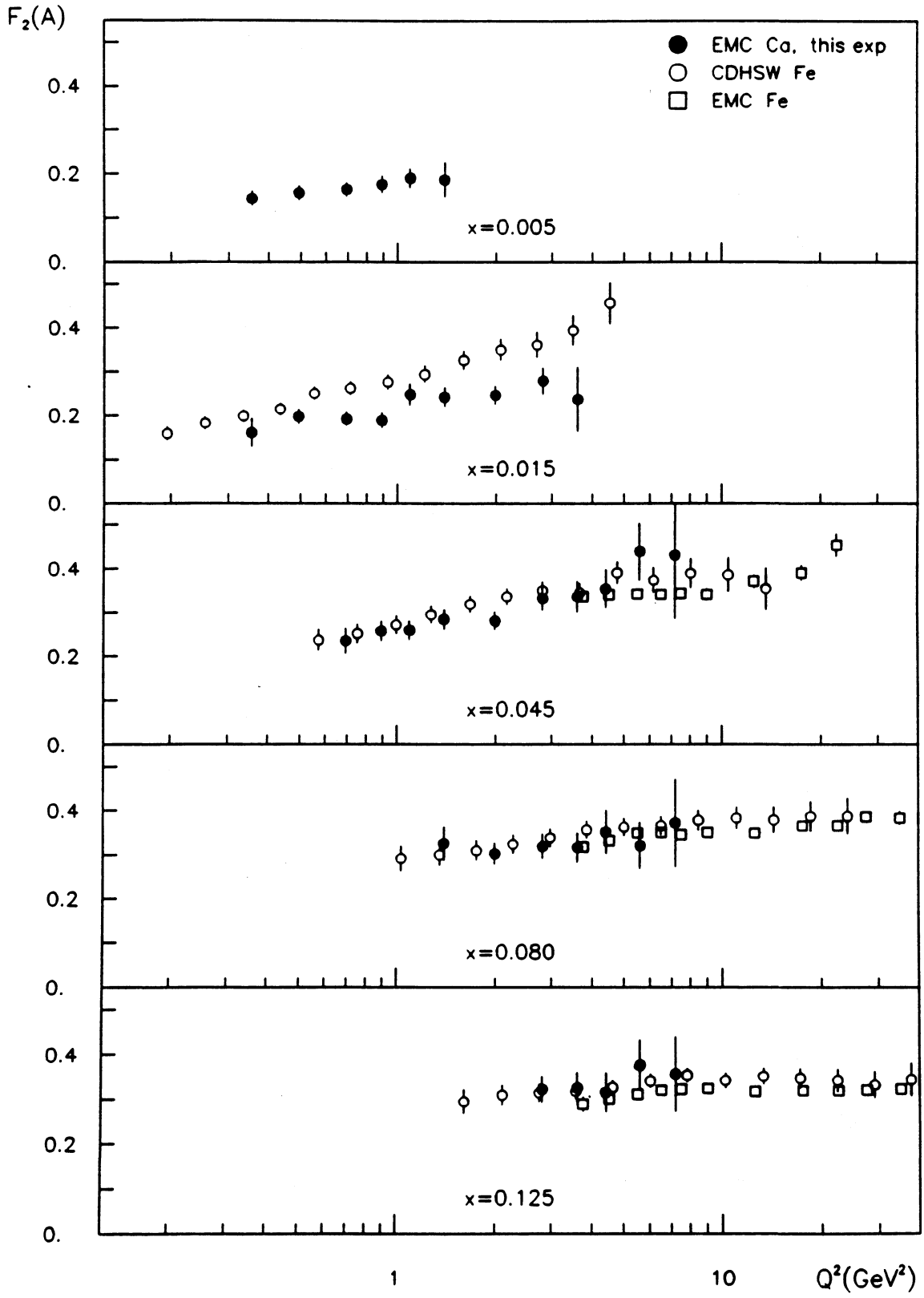
$F_2(A)$
EMC Ca, this exp
CDHSW Fe
EMC Fe
x=0.005
x=0.015
x=0.045
x=0.080
x=0.125
0.4
0.2
0.
1
10
$Q^2(GeV^2)$

Fig. 15

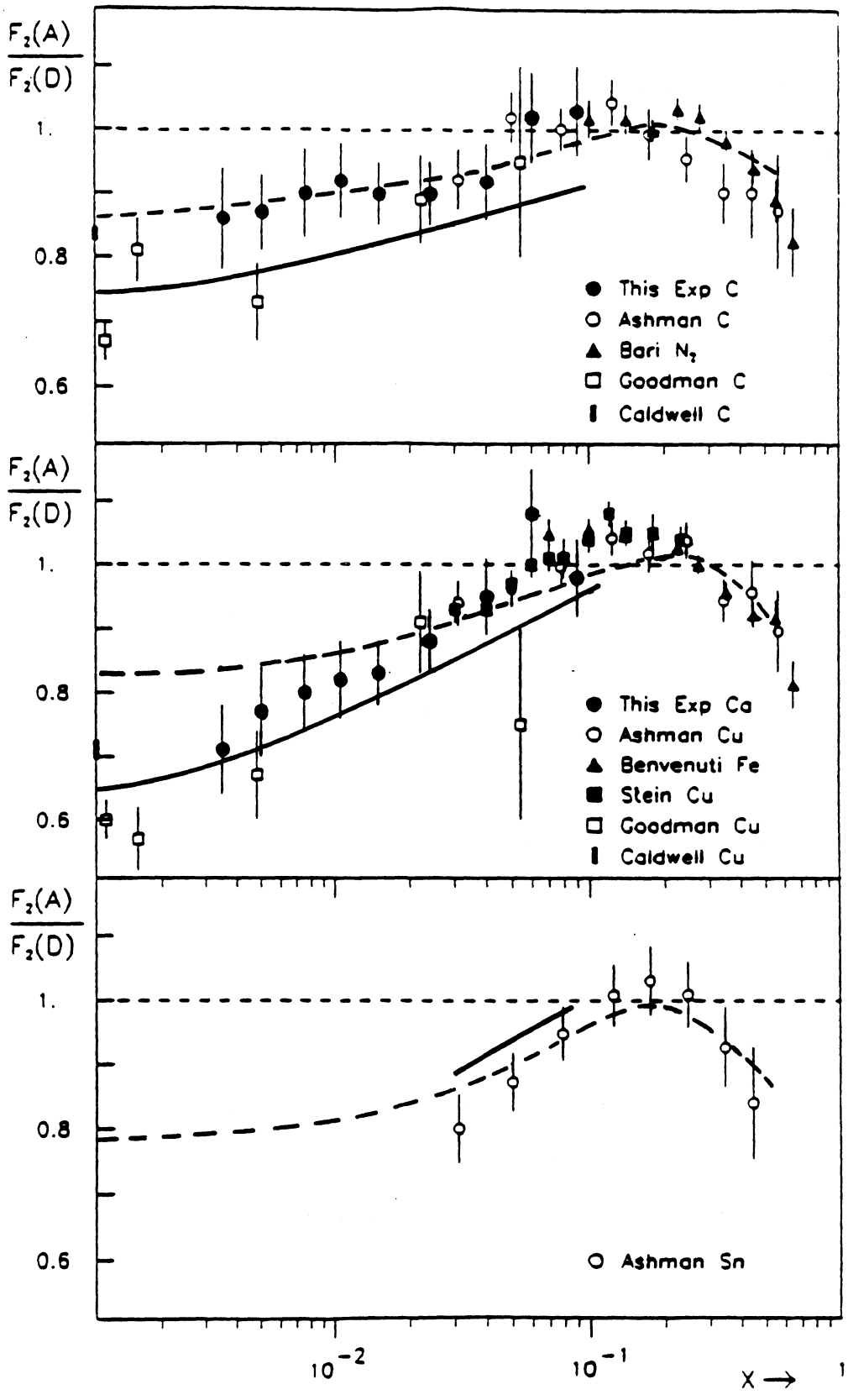
$F_2(A)/F_2(D)$
1.
0.8
0.6
This Exp C
Ashman C
Bari N_2
Goodman C
Caldwell C
$F_2(A)/F_2(D)$
1.
0.8
0.6
This Exp Ca
Ashman Cu
Benvenuti Fe
Stein Cu
Goodman Cu
Caldwell Cu
$F_2(A)/F_2(D)$
1.
0.8
0.6
Ashman Sn
10^{-2}
10^{-1}
$X \rightarrow$
1

Fig. 16

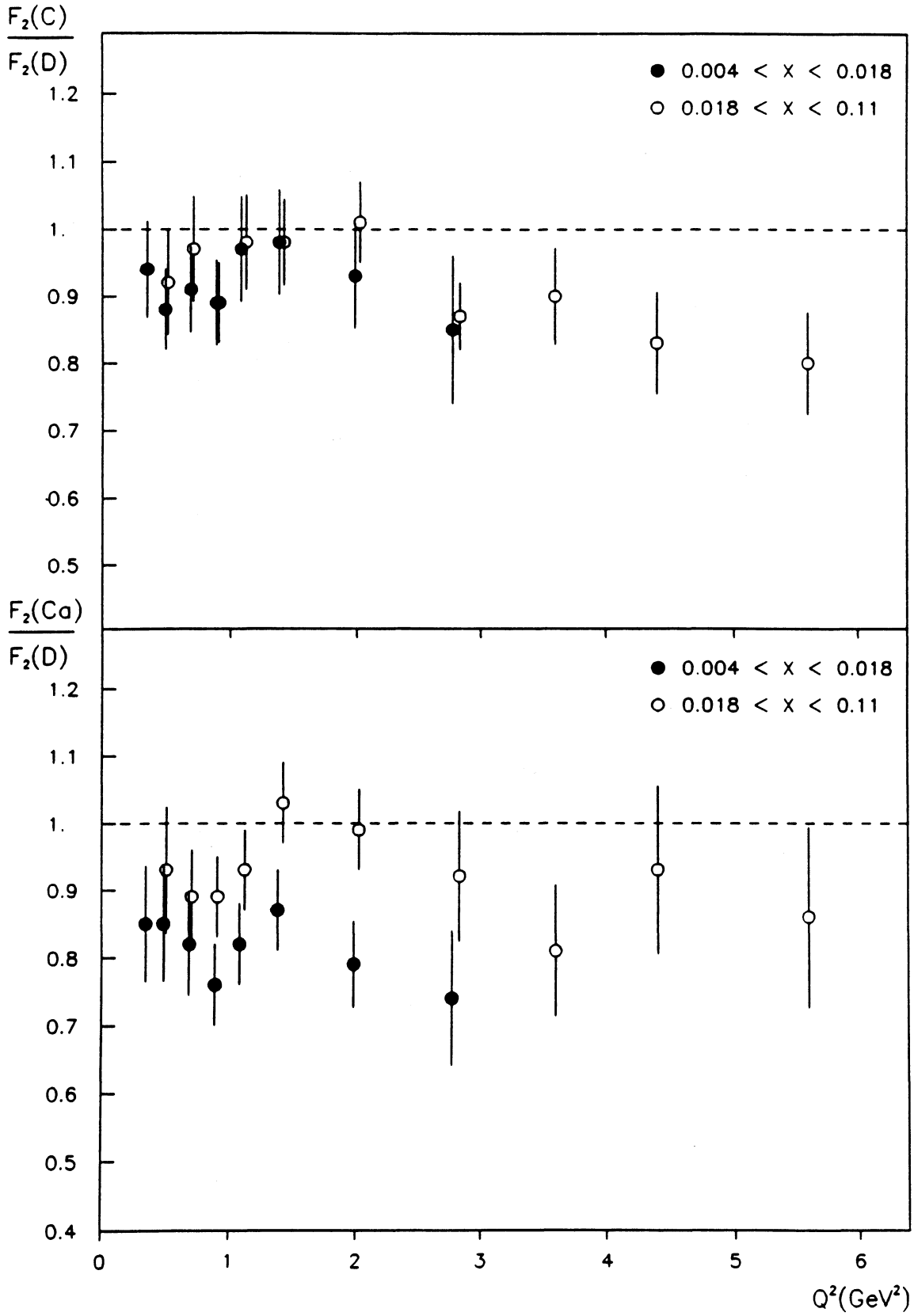
F2(C)
F2(D)
0.004 < x < 0.018
0.018 < x < 0.11
1.2
1.1
1.
0.9
0.8
0.7
0.6
0.5
F2(Ca)
F2(D)
0.004 < x < 0.018
0.018 < x < 0.11
1.2
1.1
1.
0.9
0.8
0.7
0.6
0.5
0.4
0
1
2
3
4
5
6
Q²(GeV²)

Fig. 17

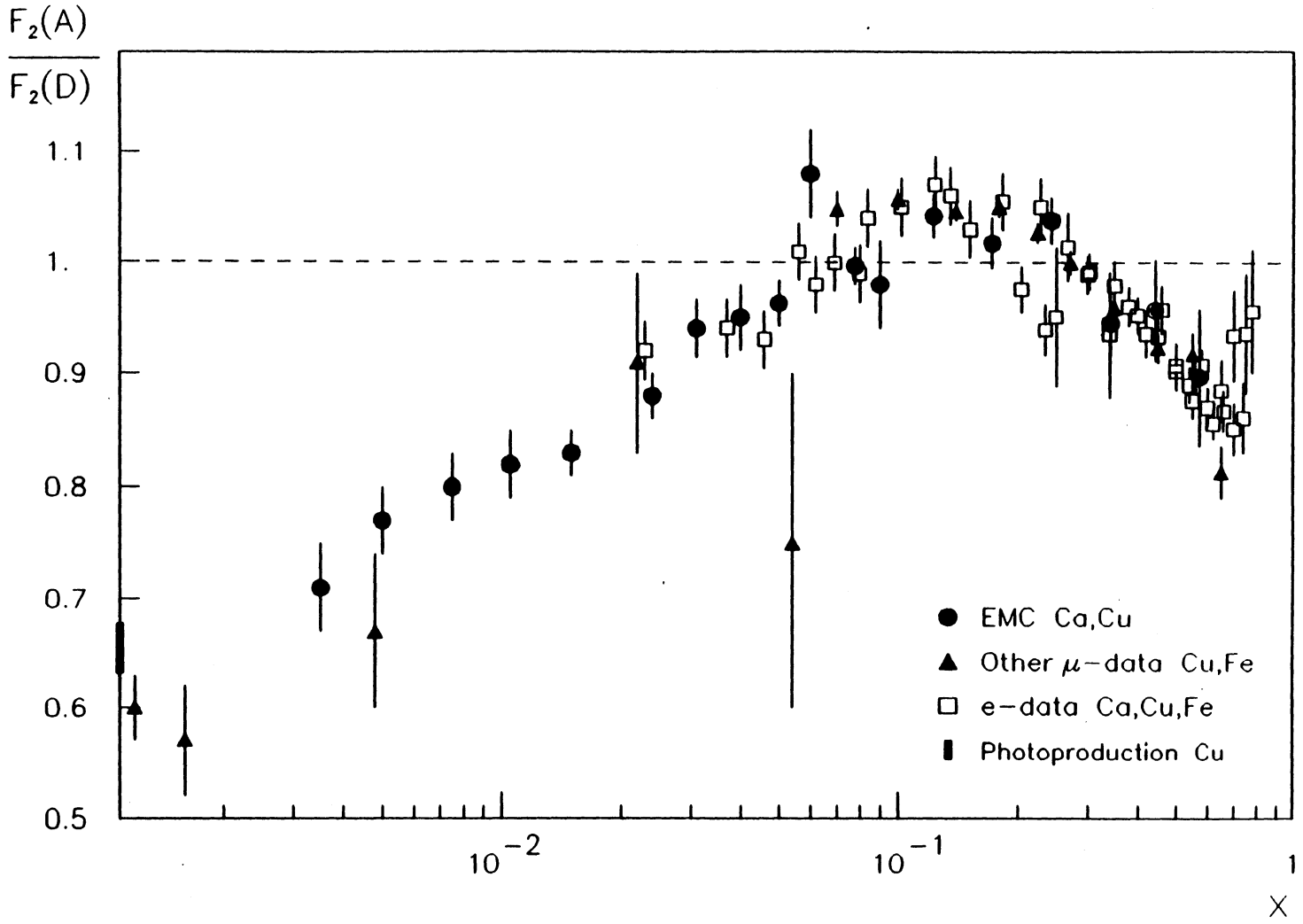
$F_2(A)$
$F_2(D)$
1.1
1.
0.9
0.8
0.7
0.6
0.5
10^{-2}
10^{-1}
1
X
EMC Ca,Cu
Other μ-data Cu,Fe
e-data Ca,Cu,Fe
Photoproduction Cu

Fig.18